Accepted Manuscript

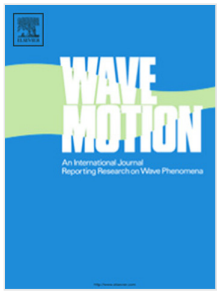

Closed crack imaging using time reversal method based on fundamental and second harmonic scattering

P. Blanloeuil, L.R.F. Rose, J.A. Guinto, M. Veidt, C.H. Wang

PII: S0165-2125(16)30065-8
DOI: http://dx.doi.org/10.1016/j.wavemoti.2016.06.010
Reference: WAMOT 2068

To appear in: *Wave Motion*

Received date: 11 February 2016
Revised date: 10 June 2016
Accepted date: 16 June 2016

Please cite this article as: P. Blanloeuil, L.R.F. Rose, J.A. Guinto, M. Veidt, C.H. Wang, Closed crack imaging using time reversal method based on fundamental and second harmonic scattering, *Wave Motion* (2016), http://dx.doi.org/10.1016/j.wavemoti.2016.06.010

Closed crack imaging using time reversal method based on fundamental and second harmonic scattering

P.Blanloeuil[a,b,*], L. R. F. Rose[b], J. A. Guinto[b], M. Veidt[a], C. H. Wang[b]

[a] *School of Mechanical & Mining Engineering, University of Queensland, Brisbane, QLD 4072, Australia*
[b] *Sir Lawrence Wackett Aerospace Research Centre, School of Engineering, RMIT University, GPO Box 2476, Melbourne, Victoria 3001, Australia*

Abstract

A recent variant of time reversal imaging is employed for reconstructing images of a closed crack, based on both the fundamental and the second harmonic components of the longitudinal scattered field due to an incident longitudinal wave. The scattered field data are generated by a finite element model that includes unilateral contact with Coulomb friction between the crack faces to account for the Contact Acoustic Nonlinearity. The closure state of the crack is controlled by specifying a pre-stress between the crack faces. The knowledge of the scattered field at the fundamental (incident) frequency and the second harmonic frequency for multiple incident angles provides the required inputs for the imaging algorithm. It is shown that the image reconstructed from the fundamental harmonic closely matches the image that is obtained from scattering data in the absence of contact, although contact between the crack faces reduces the amplitude of the scattered field in the former case. The fundamental harmonic image is shown to provide very accurate estimates of crack length for low to moderate levels of pre-stress. The second harmonic image is also shown to provide acceptable estimates of crack length and the image is shown to correlate with the source location of second harmonic along the crack, which becomes increasingly localized near the crack tips for decreasing levels of pre-stress. The influence of the number of sensors on the image quality is also discussed in order to identify the minimum sensors number requirement. Finally, multiple frequency imaging is performed over a fixed bandwidth to assess the potential improvement of the imaging algorithm when considering broadband information.

Keywords: Nonlinear Acoustics, Time Reversal Imaging, Second harmonic, Finite Element, Closed crack

1. Introduction

Early detection and characterisation of structural damage is of prime interest for effective structural integrity management. Nonlinear ultrasonics has attracted considerable attention recently because it offers

*Corresponding author
Email address: philippe.blanloeuil@rmit.edu.au (P.Blanloeuil)

the possibility of detecting various forms of material and structural damage earlier than can be achieved by conventional linear ultrasonics. The present work is concerned with cases where the source of nonlinearity can be attributed to localised contact within planar defects such as cracks and delaminations, which is referred to as contact acoustic nonlinearity (CAN) [1–5], as distinct from cases where the nonlinearity is distributed throughout the bulk of the material, due, for example, to distributed fatigue damage [6–9]. The focus of current research has evolved from simply aiming to detect the presence of CAN to the more ambitious aim of imaging the damage, *i.e.* being able to locate and size the damage, and, ultimately, of assessing the severity and the structural significance of the damage. This paper combines a recent comparative evaluation of imaging algorithms [10, 11] with a high-fidelity computational model of CAN [12–14], with the objective of assessing the image quality that can be achieved when using as input data either the fundamental or the second harmonic component of the scattered field due to a toneburst excitation. The resulting images can be expected to provide a benchmark for what could be achieved in practice, where it is not always possible to satisfy the imaging requirements of a full-view configuration, or of adequate sampling of the scattered field, and where the input data is inevitably contaminated by measurement noise.

Three imaging algorithms were rigorously evaluated and compared in [10], viz. (i) generalised diffraction tomography [15–17], also known as linearised inverse scattering [18]; (ii) beamforming [19–21], also known as delay-and-sum [22], synthetic aperture focusing technique (SAFT) [23, 24], total focusing method [25–27]; and (iii) reverse time migration [28–30] or time reversed imaging [31–33]. It was noted in [10] that only (i) has a rigorous mathematical basis, whereas (ii) and (iii), though widely used in practice, are based on heuristic arguments. A modified form of reverse time migration was formulated in [10] and recommended for practical application because it combines the ease of implementation of (ii) and (iii) with the correct point-spread-function of (i). This modified time reversal (MTR) algorithm was further investigated in [11, 34, 35], and it will be used in the present work.

Previous attempts at nonlinear ultrasonic imaging can be divided into two groups depending on whether the image reconstruction process involves (i) a point by point scanning of the ultrasonic response at every point (or pixel) within a prescribed imaging domain, usually (but not necessarily) using a laser vibrometer [36–47], or (ii) implementing an imaging algorithm that uses as input the measurements recorded by a sensor array deployed around and outside the imaging domain [48–65]. The present work belongs to the second group, which is of greater interest for structural health monitoring based on built-in sensor arrays. Nevertheless, it is pertinent to comment briefly on some aspects of the work in the first group, to further clarify the difference with the present work. In [37–42], time reversal is used as an experimental technique to achieve array focusing at a given point, the response at that point being then measured directly and processed to extract the value of the image at that point. The premise in this approach is that the chosen measure of nonlinearity that is being used to construct the image will attain a maximum value at the location

of the source of nonlinearity. However, the computational results presented in [40] indicate that this premise is not verified, because the maximum is found at 3mm away from a crack, which is the only source of CAN in the model. This highlights the value of simulations in guiding the design and interpretation of experiments. It is also noted that the MTR algorithm entails a synthetic focusing (based on time reversal), rather than the operation of a time reversal mirror to achieve a physical focusing, as used in [39, 40] and related work.

Several strategies have been proposed for nonlinear ultrasonic imaging within the second group, *i.e.* where the image is constructed via an algorithm utilising remotely acquired data. Kazakov et al. [53] and Jiao et al. [54] employed conventional imaging techniques (B-scan and beamforming, respectively), but with a superimposed low-frequency vibration. The imaging strategy is that the response from linear scatterers is not affected by the vibration, whereas the response from nonlinear scatterers depends on the instantaneous stress level during the vibration cycle, so that by subtracting images obtained at the peak and at the trough of the vibration cycle, one is left with an image of only the nonlinear scatterers, because the image of linear scatterers would cancel out during the subtraction. A related strategy is proposed by Potter et al. [56] who note that the response of a nonlinear scatterer to a parallel (*i.e.* simultaneous) transmission from a phased array, with appropriate time delays to focus on a chosen location, is different from the sum of the responses using sequential transmission, because the nonlinear response does not vary linearly with the amplitude of the input excitation. However, their approach for exploiting this difference involves choosing a suitable delay time that represents a compromise between maximising the response amplitude and establishing diffuse field conditions due to multiple boundary reflections. This choice would appear to require a trial-and-error approach. Ohara et al. [57–59] have proposed phased-array imaging of the subharmonic response generated by partially closed cracks in fatigue-cracked specimens when the input amplitude exceeds a threshold of around 50 nm, and they demonstrated an enhanced selectivity by subtracting images obtained at different values of applied load. In a recent extension of that approach, the MUSIC (Multiple Signal Classification) algorithm was used to obtain sharper images [60]. The strategy pursued in the present work is most closely related to that originally proposed in [61, 62], which is to use a higher harmonic component of the scattered field as the input to an imaging algorithm based on time reversal. However, [61] does not provide an explicit imaging condition, whereas [62] employs the DORT (French acronym for Decomposition of the Time Reversal Operator) algorithm which is appropriate for well-resolved point-like scatterers, *i.e.* scatterers that are individually small compared with the wavelength, and spaced sufficiently far apart for multiple scattering contributions to be negligible; (see [66] for a brief review). By contrast, the MTR algorithm is suitable for extended scatterers, albeit subject to the applicability of the distorted-wave Born approximation [16].

Theoretical analyses of CAN have often been based on simplified models for the contact dynamics that have nevertheless provided valuable insights for designing and interpreting experimental studies [1–5]. However, several more detailed models have also been studied, based on different computational approaches, viz.

(i) hypersingular integral equations [67, 68]; (ii) time-domain finite difference [69, 70]; and (iii) finite-element (FE) method [12, 14, 40, 71]. The present work uses the open source FE package Plast2 [72, 73] as already used in [12, 14], which has the particularity to make use of the Lagrange multipliers method to solve the contact problem in a robust way.

As noted earlier, the objective of this work is to document the imaging performance that can be achieved by using either the fundamental or the second harmonic component of the scattered field as input to the MTR imaging algorithm. The presentation is organised as follows. Section 2 describes the imaging configuration and Section 3 the imaging algorithm. The FE model is presented in Section 4 followed by a verification of certain properties of the scattered field that are exploited for imaging purposes. This FE model is for a 2D plane strain analysis, but it seems reasonable to expect that the general results summarised in the conclusion, Section 6, will also apply for Lamb wave imaging, thereby providing a valuable extension to nonlinear imaging of recent advances in linear Lamb-wave imaging [11, 17, 74–76]. The MTR algorithm may also provide an attractive alternative to the probabilistic RAPID algorithm [77, 78] that has been used in [65] for imaging surface corrosion based on the nonlinear component of Rayleigh-wave scattering detected by a surface-mounted active sensor array.

2. Problem statement

An homogeneous isotropic material is considered in a 2D configuration. This configuration is useful for deriving the imaging algorithm [10, 15, 18]. In the present work, this configuration corresponds to a section of a large width bulk solid. This solid contains a crack closed by a superimposed compressive stress σ_0. The origin of the coordinate system is chosen to coincide with the center of the crack, as shown in Fig. 1. An imaging domain is defined around the defect and is indicated by the gray area in Fig. 1. N sensors are distributed along a closed curve Γ that encloses the imaging domain. For simplicity, a circular sensors array of radius R is considered in this work.

In the FE model described later in Section. 4.1, an incident longitudinal plane wave of angular frequency ω_1 is generated in the far field and propagates such that the incident wave vector is collinear with $\overrightarrow{X_jO}$. In other words, the propagation path from the sensor X_j to the origin defines the direction of propagation for the incident plane wave. For the sake of simplicity, X_j is referred to an actuator in the following. The incident wave interacts with the closed crack where unilateral contact with Coulomb friction is considered to model CAN. This interaction results in the scattering of different waves that are recorded by N sensors X_i, which are in this case proper point-like receivers.

For a given incident wave, the scattered field consists of longitudinal waves and shear waves as indicated in Fig. 1. Because of the CAN, each of these scattered waves has an enriched frequency content that contains the incident frequency ω_1 (fundamental harmonic) and multiples of the incident frequency $\omega_2, \omega_3, ...$ (higher

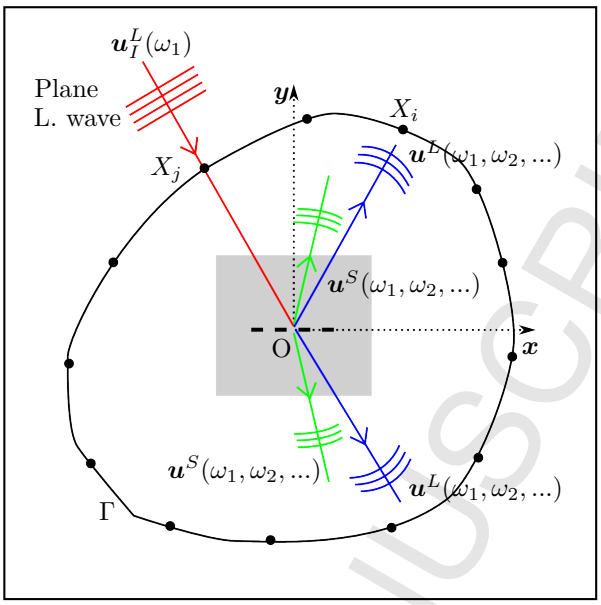

Figure 1: Schematic of the imaging problem where the closed crack (dashed line) is located at the origin of the coordinate system. Sensors (solid circles) are placed around the imaging domain, which is defined by the gray square. A plane longitudinal wave is incident along the direction $\overrightarrow{X_jO}$, and the sensors X_i record the scattered waves for a complete range of scattering angles.

harmonics) [14].

The objective of this paper is to use either the fundamental or the second harmonic of the scattered field to reconstruct an image of the closed crack by means of time reversal imaging. The scattered field $\boldsymbol{u}$ is extracted from a two-step procedure in which the solid is first interrogated without the crack to obtain the baseline $\boldsymbol{u}_B$, and a second time with the crack to obtain the total field $\boldsymbol{u}_T$. Considering the wave emission from X_j, the scattered field for each receiver X_i is then defined as the difference between the total field and the baseline:

$$\boldsymbol{u}(X_j, X_i, t) = \boldsymbol{u}_T(X_j, X_i, t) - \boldsymbol{u}_B(X_j, X_i, t) \tag{1}$$

For simplicity, only the longitudinal scattered waves are considered here and the mode converted shear waves are disregarded. This assumes that the longitudinal scattered waves can be separated from the scattered shear waves for sensors X_i in the time domain. The incident wave is taken to be a 5-cycle tone-burst defined by a Hann window. The same duration Hann window is used to isolate the scattered longitudinal waves based on the knowledge of the time of flight of the longitudinal wave from the origin to the receiver. The scattered longitudinal field is denoted:

$$\boldsymbol{u}^L(X_j, X_i, t). \tag{2}$$

At this stage, the displacement field of the longitudinal scattered wave is expressed in the Cartesian

coordinate system, with components u_x and u_y. In a polar coordinate system, a longitudinal wave scattered from the origin generates mostly radial displacements u_r. Tangential displacements are also generated due to Poisson's effect. In the imaging algorithm introduced later, the radial component u_r^L is considered as the quantity defining the scattering of a longitudinal wave. This choice is possible based on the following assumptions: (i) the longitudinal wave can be separated from the shear wave, and (ii) the scattered displacements created by the longitudinal wave are collinear with the radial direction and the associated tangential displacement is negligible. The possibility of time gating the scattered longitudinal waves, and the quality of the radial displacements corresponding to the scattered longitudinal waves, will be discussed in section 4.2.

The problem considered here is to reconstruct the defect based on the knowledge of the scattered field at all receivers for all actuators considered successively:

$$\boldsymbol{u}_r^L(X_j, X_i, t), \quad 1 \leq i, j \leq N \tag{3}$$

3. Modified Time Reversal imaging

The data collected from $N \times N$ actuator-receiver pairs is used to reconstruct the defect image using time reversal imaging algorithm. Although the scattered field data is necessarily recorded in the time domain, the imaging algorithms are more easily derived and implemented in the frequency domain [10]. Therefore, the first step prior to applying the imaging formula consists in converting the scattered field to the frequency domain by applying the Fourier transform. The scattered field (for the radial displacement) is thus denoted

$$\hat{u}_r^L(X_j, X_i, \omega). \tag{4}$$

The knowledge of the scattering data from all actuator-receiver pairs enables one to construct the so-called multi-static data matrix [10] $\boldsymbol{K}$ at frequency ω defined by:

$$K_{ij}(\omega) = \hat{u}_r^L(X_j, X_i, \omega), \quad 1 < j, i < N. \tag{5}$$

i.e. $K_{ij}(\omega)$ denotes the value of the Fourier transform at frequency ω for the scattered field at X_i due to an input at X_j, with the further restriction in the present work that only the longitudinal component of the scattered displacement field is being used for the purposes of imaging. The multi-static matrix thus contains all information resulting from the interaction between the incident waves and the crack, and therefore is the core input for the imaging algorithm.

Fig. 2 introduces the different notations required to derive the imaging formulae. A circular array of sensors and a square imaging domain are considered, their respective centers are concurrent with the crack center, which defines the origin of the coordinate system. The sensor positions are defined using polar coordinates (ρ, φ) relative to an imaging point $\boldsymbol{x}$, as shown in Fig. 2(b).

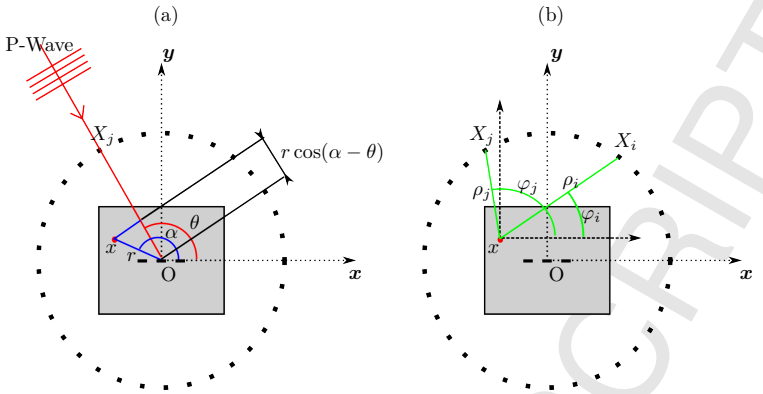

Figure 2: Configuration of the sensors, closed crack and imaging domain, with the incident plane wave (a), and the definition of the polar coordinates of sensors relative to an imaging point $\boldsymbol{x}$ (b).

Considering a 2D acoustic model where the time dependence is chosen to be $e^{-i\omega t}$, the waves propagating from a point source satisfy the following 2D scalar wave equation, which is given in the frequency domain:

$$\nabla^2 \hat{u} + k^2 \hat{u} = -\hat{p}(\omega)\delta(\boldsymbol{x} - \boldsymbol{X}_j), \tag{6}$$

where $k = \omega/c$ denotes the wavenumber in the background medium with c being the phase velocity of the considered wave, and $\hat{p}(\omega)\delta(\boldsymbol{x} - \boldsymbol{X}_j)$ describes a point-like source at actuator X_j. The incident field received at $\boldsymbol{x}$ from the source $\boldsymbol{X}_j$ is given by

$$\hat{u}(\boldsymbol{x}, \boldsymbol{X}_j, \omega) = \hat{p}(\omega) G(\boldsymbol{x}, \boldsymbol{X}_j, \omega), \tag{7}$$

where $G(\boldsymbol{x}, \boldsymbol{X}_j, \omega)$ is the Green's function for frequency ω, which is by definition the solution for the wave propagation due to a point-like Dirac excitation. To satisfy the Sommerfeld radiation condition, the Green's function for this propagation problem is given by [15, Chapter 6]:

$$G(\boldsymbol{x}, \boldsymbol{X}_j, \omega) = \frac{i}{4} H_0^{(1)}(k|\boldsymbol{x} - \boldsymbol{X}_j|), \tag{8}$$

where, $H_0^{(1)}$ denotes the zero order Hankel function of the first kind, and $|\boldsymbol{x} - \boldsymbol{X}_j|$ corresponds to the propagation distance from the source to the considered point $\boldsymbol{x}$.

As noted in section 2, the incident wave in the FE model is generated as a plane wave propagating along the direction $\overrightarrow{X_j O}$, rather than a point source as assumed in the acoustic model. This is appropriate for modelling Fig. 2(a) provided that the source point X_j can be considered to be in the far field relative to the imaging domain, which is assumed to be the case in the present work. By definition, this incident plane wave does not present any cylindrical spreading and is assumed to maintain a constant amplitude. Thus, only the phase difference between the actuator $\boldsymbol{X}_j$ and the imaging point $\boldsymbol{x}$ needs to be considered to describe the propagation of the incident wave, i.e. the incident wave is given by:

$$\hat{\boldsymbol{u}}^I(\boldsymbol{x}, \boldsymbol{X}_j, \omega) = e^{ikr\cos(\alpha-\theta)} \tag{9}$$

where r is the distance between the origin and the imaging point, and α, θ are respectively the angular coordinates for the imaging point and the actuator, as shown in Fig. 2. In the following, the notation $G(\boldsymbol{x}, \boldsymbol{X}_j, \omega) = \hat{\boldsymbol{u}}^I(\boldsymbol{x}, \boldsymbol{X}_j, \omega)$ will be used to account for the propagation of the incident wave.

Considering the propagation from the imaging point $\boldsymbol{x}$ to the receiver $\boldsymbol{X}_i$, the definition of the Green's function defined by Eq. 8 is correct. For large argument $k|\boldsymbol{x} - \boldsymbol{X}_i| \gg 1$, the asymptotic expansion of the Hankel function [79] leads to the following expression:

$$G(\boldsymbol{x}, \boldsymbol{X}_i, \omega) \simeq \sqrt{\frac{i}{8\pi k|\boldsymbol{x} - \boldsymbol{X}_i|}} e^{ik|\boldsymbol{x}-\boldsymbol{X}_i|}, \text{for } k|\boldsymbol{x} - \boldsymbol{X}_i| \gg 1. \tag{10}$$

In practice, this formula provides an excellent approximation even for $|\boldsymbol{x}-\boldsymbol{X}_i| \geq 2\lambda$, where λ is the wavelength of the considered wave [10]. This requirement is satisfied in the present work, so that Eq. 10 will be used to describe the propagation from the imaging point to the receiver for the imaging algorithm.

Rose at al. have derived a general time reversal imaging formula based on the acoustic model and a cross-correlation imaging condition [10]. The multi-static data is assumed to be known, and the reconstructed image is given by:

$$S_{TR}(\boldsymbol{x}, \omega) = 8\pi k \int_0^{2\pi} \left\{ \int_0^{2\pi} \boldsymbol{K}_{ij}^* G(\boldsymbol{x}, \boldsymbol{X}_i, \omega) \rho_i d\varphi_i \right\} G(\boldsymbol{x}, \boldsymbol{X}_j, \omega) \rho_j d\varphi_j, \tag{11}$$

where the asterisk denotes the complex conjugation. For theoretical purposes, this first imaging formula assumes a continuous sensor distribution. The terms ρ_i, ρ_j and φ_i, φ_j are respectively the distances and the incline angles between the imaging point $\boldsymbol{x}$ and the sensors $\boldsymbol{X}_i$ and $\boldsymbol{X}_j$, as defined in Fig. 2.

Unlike diffraction tomography, Eq. 11 can be applied for near-field imaging. However, to ensure that Eq. 11 correctly reduces to diffraction tomography in the far field limit, Rose et al. have proposed a Modified Time Reversal formula [10] given by:

$$S_{MTR}(\boldsymbol{x}, \omega) = 8k^4 \int_0^{2\pi} \left\{ \int_0^{2\pi} \boldsymbol{K}_{ij}^* G(\boldsymbol{x}, \boldsymbol{X}_i, \omega) |\sin(\varphi_i - \varphi_j)| \rho_i d\varphi_i \right\} G(\boldsymbol{x}, X_j, \omega) \rho_j d\varphi_j, \tag{12}$$

where the term $|\sin(\varphi_i - \varphi_j)|$ arises from the Jacobian of the transformation [15, Chapter 6] between the integration variables in $\boldsymbol{k}$-space and the angles φ_i, φ_j defined in Fig. 2.

In practice, there is a discrete distribution of sensors, and the double integral in Eq. 12 is evaluated as a double sum:

$$S_{MTR}(\boldsymbol{x}, \omega) = \frac{32\pi^2 k^4}{N^2} \sum_{i=1}^{N} \sum_{j=1}^{N} \boldsymbol{K}_{ij}^* G(\boldsymbol{x}, \boldsymbol{X}_i, \omega) G(\boldsymbol{x}, \boldsymbol{X}_j, \omega) |\sin(\varphi_i - \varphi_j)| \rho_i \rho_j. \tag{13}$$

As introduced previously, this work intends to image a closed crack using either the fundamental harmonic or the second harmonic contained in the scattered waves. The considered frequency components being different, the wave numbers have to be modified accordingly in the imaging formula. The wavenumber in Eq. 10 is chosen equal to $k = \omega_1/c$ or $k = \omega_2/c$ respectively for the imaging based on the fundamental

frequency ω_1 and second harmonic frequency $\omega_2 = 2\omega_1$, where c denotes the longitudinal wave velocity. The wavenumber of the incident wave in Eq. 9 is always $k = \omega_1/c$. The longitudinal wave velocity is defined by:

$$c = \sqrt{\frac{(1-\nu)E}{(1+\nu)(1-2\nu)\rho}}, \tag{14}$$

where ν, E and ρ are respectively Poisson's ratio, the Young's modulus and the density of the material.

In the following, the imaging based on the fundamental harmonic is referred as "fundamental harmonic imaging" whereas the imaging based on the second harmonic is denoted by "second harmonic imaging". The two corresponding formula are given by:

$$S_{MTR}(\boldsymbol{x}, \omega_1) = \frac{32\pi^2 k^4}{N^2} \sum_{i=1}^{N} \sum_{j=1}^{N} \boldsymbol{K}^*_{ij}(\omega_1) G(\boldsymbol{x}, \boldsymbol{X}_i, \omega_1) G(\boldsymbol{x}, \boldsymbol{X}_j, \omega_1) |\sin(\varphi_i - \varphi_j)| \rho_i \rho_j \tag{15a}$$

$$S_{MTR}(\boldsymbol{x}, \omega_2) = \frac{32\pi^2 k^4}{N^2} \sum_{i=1}^{N} \sum_{j=1}^{N} \boldsymbol{K}^*_{ij}(\omega_2) G(\boldsymbol{x}, \boldsymbol{X}_i, \omega_2) G(\boldsymbol{x}, \boldsymbol{X}_j, \omega_1) |\sin(\varphi_i - \varphi_j)| \rho_i \rho_j \tag{15b}$$

where S_{MTR} is a complex value that corresponds to the damage intensity. Note that the imaging algorithm can be formulated for any higher harmonic or side-band frequency components generated in case of nonlinear wave modulation. The choice of the second harmonic for the present study follows partly from previous work [13, 14] characterising the scattering patterns of second and third harmonics, and partly from the expectation that the second harmonic may suffice for characterising CAN.

In this paper, the image intensity at location $\boldsymbol{x}$ and frequency ω_i is defined as the absolute value of S_{MTR} normalized by its maximal amplitude:

$$I_{MTR}(\boldsymbol{x}, \omega_i) = \frac{|S_{MTR}(\boldsymbol{x}, \omega_i)|}{\max |S_{MTR}(\boldsymbol{x}, \omega_i)|}, \quad i = 1, 2. \tag{16}$$

The MTR imaging formula has been defined, with Green's functions adjusted to the considered problem. The next section introduces the FE model that enables to treat the nonlinear interaction between an incident plane wave and a closed crack.

4. Finite Element modeling and validation

This section describes firstly the FE model used to model the nonlinear interaction between the incident plane wave and the closed crack and secondly validates the assumptions regarding the scattered longitudinal wave field.

4.1. FE model

A plane strain 2D FE model is set up to tackle the nonlinear interaction between an incident longitudinal plane wave and a closed crack. As done previously in [14], the CAN is taken into account by unilateral

contact with Coulomb's friction and the FE code Plast2 [72, 73] is used to solve the problem. This model enables to compute the acoustic field scattered by the crack for various angles of incidence, which eventually provides the multi-static data matrix used as an input for the imaging algorithm introduced in section 3.

The particular configuration of the FE model is shown in Fig. 3. A square aluminum solid is considered, with mechanical properties defined by the Young's modulus $E = 69$ GPa, the Poisson's coefficient $\nu = 0.33$ and the density $\rho = 2700$ kg.m^{-3}. This solid contains a crack of length $d = 10$ mm that may be tilted by an angle α, and whose center defines the origin of the coordinate systems. Perfectly Matched Layers (PML) of 10 mm thickness are set around the solid to prevent reflections, thereby simulating an infinite medium. A longitudinal plane wave of frequency $f_1 = 1$ MHz and amplitude $A = 10$ nm is generated in the solid by imposing normal displacements on the top face. This wave is a 5-cycle sinusoidal tone burst windowed by a Hann window. It propagates at the velocity $c = 6153$ m/s, which gives a wavelength of $\lambda \simeq 6$ mm. In aluminum, the maximal value of the stress $|\sigma_{yy}|$ generated by the incident wave is approximatively 1 MPa.

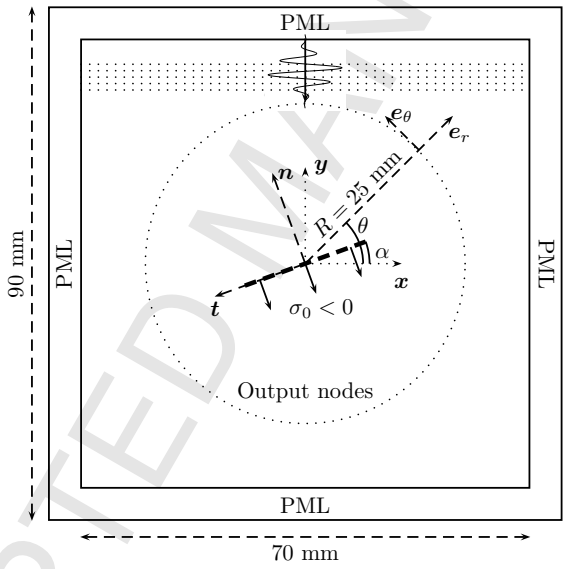

Figure 3: Modeling of a wave interacting with a crack orientated by the angle α. The length of the crack is $d = 10$ mm. The crack is represented by the thick dashed line and a pre-stress σ_0 is applied on the interface. The numerical output is defined on a circle of radius $R = 25$ mm.

The incident wave interacts with the crack, which is modeled as a contact interface, where a potential compressive pre-stress $\sigma_0 \leq 0$ is considered to close the interface. A coefficient of friction $\mu = 0.3$ is considered if not stated otherwise. The contact interface is modeled using unilateral contact law with Coulomb friction which represents a simplified model of the contact interface that captures the essential contribution of contact dynamics to the scattering response as done previously in [14, 68]. The contact equations are recalled here for completeness.

The two faces of the crack are denoted by $i = 1, 2$ respectively for the top and bottom face. As proposed in [73], let be $\boldsymbol{u}^i$ the displacement and $\boldsymbol{n}^i$ the outward normal vector of the face i of the crack. The normal jump of displacements is then defined by:

$$[u_n] = \boldsymbol{u}^1 \cdot \boldsymbol{n}^1 + \boldsymbol{u}^2 \cdot \boldsymbol{n}^2 = (\boldsymbol{u}^1 - \boldsymbol{u}^2) \cdot \boldsymbol{n}^1 \tag{17}$$

The incident wave creates stresses represented by the Cauchy stress tensor $\boldsymbol{\sigma}(\boldsymbol{u}^i)$. Denoting by $\sigma_n(\boldsymbol{u}^i)$ its normal component and by $\tau(\boldsymbol{u}^i)$ its tangential component on the crack faces, the unilateral contact law taking into account σ_0 is given by the following equation:

$$\begin{cases} \sigma_n(\boldsymbol{u}^i) + \sigma_0 \leq 0 \\ [u_n] \leq 0 \\ (\sigma_n(\boldsymbol{u}^i) + \sigma_0).[u_n] = 0 \end{cases} \tag{18}$$

The first equation states that only a compression can be transmitted through the interface. The normal stress σ_n is allowed to be positive although the crack is closed as long as $\sigma_n \leq \mid \sigma_0 \mid$. When $\sigma_n = -\sigma_0$ the interface opens. The second line corresponds to the nonpenetration condition. Finally, the third line, or complementary equation, indicates that the contact interface is either open or closed.

Denoting μ the friction coefficient and $[u_t]$ the tangential jump of displacements, the Coulomb's law is used for the tangential behavior. The pre-stress σ_0 is also introduced in the classical law:

$$\begin{cases} \mid \tau(\boldsymbol{u}^i) \mid \leq \mu \mid \sigma_n(\boldsymbol{u}^i) + \sigma_0 \mid \\ \text{If } \mid \tau(\boldsymbol{u}^i) \mid < \mu \mid \sigma_n(\boldsymbol{u}^i) + \sigma_0 \mid \Rightarrow \text{ sticking: } [u_t] = 0 \\ \text{If } \mid \tau(\boldsymbol{u}^i) \mid = \mu \mid \sigma_n(\boldsymbol{u}^i) + \sigma_0 \mid \Rightarrow \begin{cases} \text{sliding: } \exists \alpha \geq 0; [u_t] = -\alpha \tau(\boldsymbol{u}^i) \\ \tau(\boldsymbol{u}^i) = \pm \mu \mid \sigma_n(\boldsymbol{u}^i) + \sigma_0 \mid \end{cases} \end{cases} \tag{19}$$

The shear stress τ has to be equal to $\mu \mid \sigma_n + \sigma_0 \mid$ to generate sliding. When sliding occurs, the value of the shear stress now depends on the total normal stress $\sigma_n + \sigma_0$.

The contact equations Eq. 18 and 19 have to be verified at each node belonging to the contact interface, at each time step. In Plast2, the contact algorithms are based on the forward Lagrange multipliers method [80] which enables the use of Lagrange multipliers in a time explicit integration. More precisely, the contact equations are respectively satisfied a time t and $t + \Delta t$. To make this possible, the contact equations are solved using a Gauss-Seidel iterative solver. The global method is thus semi-implicit. This method has been demonstrated to be robust [73]. The advantage of using the Lagrange multipliers is that the contact laws are strictly verified at each time step, which is of primary importance for modeling the contact dynamics generated by the incident wave propagation.

The spatial discretization is essential in the FE method. In order to have an accurate solution for the new higher frequency components generated by the CAN, the corresponding wavelengths have to be sufficiently

discretized. If i is the number of the highest harmonic considered, then the corresponding wavelength λ_i has to be divided by at least 10 elements [81]: $\lambda_i/a_{max} \geq 10$ where a_{max} is the maximal element dimension. That means that the FE mesh has to be defined depending on the highest frequency of interest. In this work, the fundamental and the second harmonic are considered. Accordingly, the maximal size of the elements is $a_{max} = 0.2$ mm which means that the wavelength of the second harmonic is divided in 15 elements ($\lambda_2/a_{max} \simeq 15$). The mesh is refined at the vicinity of the crack tips because of stress singularities, with minimal size of the elements of $a_{min} = 0.07$ mm. Having an accurate estimation of the stress concentration at the crack tip is essential in fracture mechanics but beyond the scope of this study. The mesh is made only of fully integrated quadrangle elements of type Q_1 [82]. The software Plast2 uses a time explicit integration scheme and therefore the time step is subject to the Courant-Friedrichs-Lewy stability condition $\Delta t \leq a_{min}/c$, where a_{min} corresponds to the smallest element dimension and c to the longitudinal wave velocity in the medium (Eq. 14). Convergence studies have been carried out in time and space to ensure that convergence was achieved.

An imaging domain of 25×25 mm^2 is selected. To obtain an accurate reconstruction of the defect, the Nyquist sampling criterion must be satisfied, which states that the number of sensors N must be at least equal to $2kR_0$, where R_0 is the approximate radius of the imaging area. Following this requirement, the number of sensors is set to $N = 74$ considering the wavenumber of the second harmonic, and the diagonal of the imaging domain as R_0 [10]. Those 74 sensors are equally distributed on a circle of radius $R = 25$ mm centered on the origin.

In the previous sections, it has been explained that various angles of incidence are considered depending on which sensor is chosen to define the excitation. With the current FE model, instead of defining a plane wave coming from different directions, the excitation is always generated on the top face, but the configuration is altered so that the crack is tilted by an angle α that matches the angle of incidence defined by $\overrightarrow{X_jO}$. This approach is shown in Fig. 4.

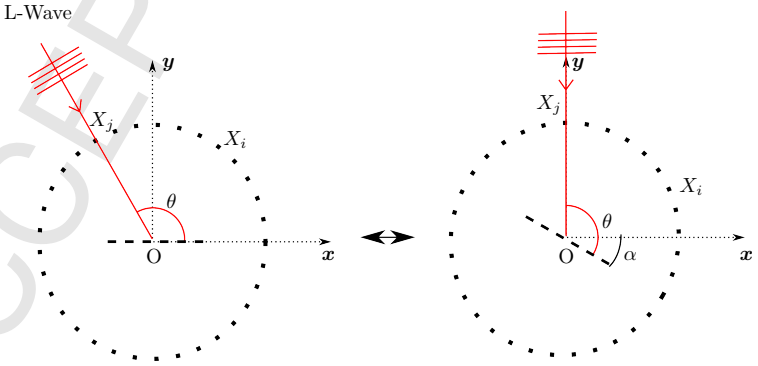

Figure 4: Definition of crack rotation to achieve various angles of incidence corresponding to each actuator X_j.

To make this possible without re-meshing the solid each time, a specific strategy was adopted to define the crack orientation as a simple input parameter of the FE model. Basically, the mesh is divided in two sections, one being a disk of radius $R = 25$ mm that contains the crack, the second being the square solid from which the inner disk has been removed. To model a particular angle of incidence, the inner disk is rotated by an angle α and put back inside the outer domain, the two parts being connected by a perfect tied contact interface that ensures continuity of displacements and stresses. Thus, it is very convenient to modify the crack orientation. This additional contact interface is evaluated only at the first iteration and therefore does not increase the computation cost of the simulation. Finally, the definition of this circular interface is convenient for the definition of 74 point-like sensors at a distance of $R = 25$ mm from the origin, which is simply done by selecting 74 equi-spaced nodes belonging to the outer face.

The scattered field is defined as the difference between the total field and the incident field (obtained without the crack). Therefore, two simulations have to be run to compute the scattered wave field: with and without the crack. The displacements recorded at the selected output nodes for each simulation are subtracted to obtain the scattered near field solution. Displacements are projected in the polar coordinate system and the longitudinal wave is selected with a Hann window of the same duration as the incident pulse. Only the radial displacement is used in the imaging algorithm. These signals are converted in the frequency domain using the FFT algorithm and the complex values are selected at the fundamental frequency and at the second harmonic. Considering all actuator-receiver pairs, two sets of data are obtained, which enables one to construct the multi-static data matrix for the fundamental harmonic and for the second harmonic, and hence to reconstruct two images in accordance with Eq. 15.

4.2. Verification of the hypothesis regarding the scattered field

The radial displacement created by the scattered longitudinal wave is used to construct the input for the imaging algorithm. As mentioned in section 2, this is based on the following assumptions regarding the scattered field: (i) the longitudinal wave can be separated from the shear wave in the time domain ; (ii) radial displacements do correspond to induced longitudinal displacements. This section demonstrates that these two conditions are verified and that the radial displacements give a sufficiently accurate description of the scattered longitudinal waves, which in turn justifies the use of the acoustic model for deriving the imaging algorithm in section 3.

Fig. 5(a) shows a snapshot of the total displacement field after the interaction of the incident wave with a crack tilted by $\alpha = 25°$. Although the baseline field has not been removed, one can clearly notice the scattered longitudinal wave followed by the mode converted shear wave. The two scattered pulses propagate with different velocities and with the maximum amplitudes along different directions. The array of sensors is marked by the dotted circle, and the output node marked by the solid red disk is selected to plot time history displacements. As shown in Fig. 5(a), this node receives successively displacements from the two scattered

modes. The corresponding displacements are plotted in Fig. 5(b). More precisely, the Cartesian displacement components u_x and u_y as well as the corresponding polar displacement components u_r and u_θ are shown for this output node. As expected, the two waves generate both u_x and u_y displacements. However, it can be seen that the two pulses are clearly separated. Furthermore, the radial component corresponds only to the longitudinal wave whereas the tangential component corresponds mainly to the shear wave. Note that it is expected that the longitudinal wave generates some tangential displacements due to the Poisson's effect. Thus, these results confirm that it is possible to separate the scattered modes in our case, and that the radial component corresponds mainly to the longitudinal wave.

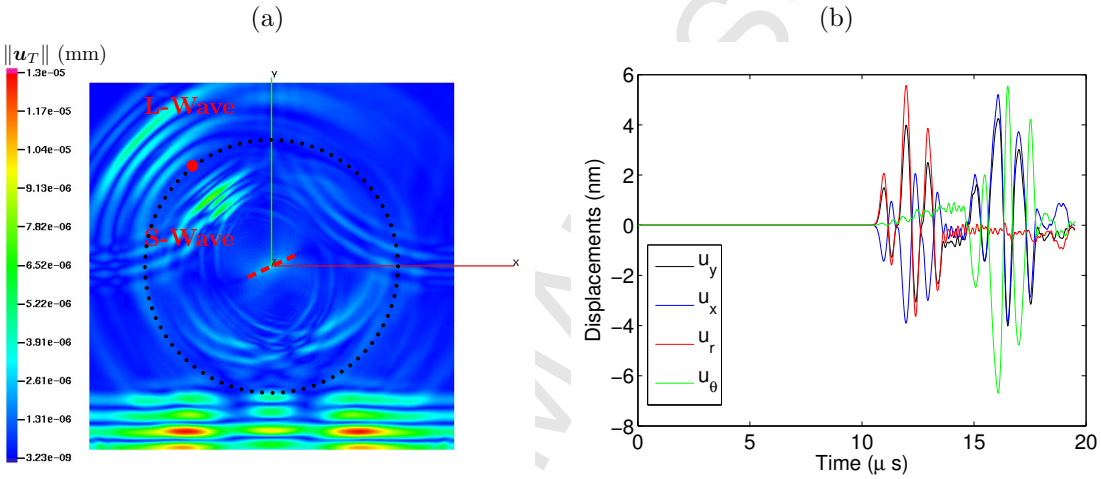

Figure 5: (a) Total displacement $\|\boldsymbol{u}_T\|$ field after interaction with the crack, at $t = 13.6$ μs. (b) displacement time signals extracted from the selected node marked by the solid red disk in (a), in Cartesian and polar coordinates.

However, the scatterer being a crack of finite length, scattered waves do not have circular wave fronts in the near field that matches the curvature of the sensor array. Therefore, the scattered longitudinal waves produce pure radial displacement only at the center of the scattered wave beam, whereas the angle between the radial direction and the displacement increases on going away from the direction of propagation. By contrast, the non-plane wave condition of the scattered longitudinal waves may introduce shear deformation that contributes to the computed radial component without corresponding to longitudinal wave motion. In the following, the radial displacement is compared with the first strain invariant to address these two issues. The first strain invariant is independent of shear deformation by definition, and therefore corresponds only to motion induced by the propagation of scattered longitudinal waves. Moreover, the first strain invariant is independent of the coordinate system.

The following general expressions are adopted for displacements,

$$\begin{cases} u_x(x,y,t) = Ae^{i(k_x x + k_y y)}e^{-i\omega t} \\ u_y(x,y,t) = Be^{i(k_x x + k_y y)}e^{-i\omega t} \end{cases} \tag{20}$$

In the following, the space and time dependence are omitted. The first strain invariant $\varepsilon_x + \varepsilon_y$ is then given by:

$$\varepsilon_x + \varepsilon_y = i(k_x u_x + k_y u_y) \tag{21}$$

with $k_x = k\cos\theta$ and $k_y = k\sin\theta$, where k is the wave number of the longitudinal wave and θ gives the direction of propagation. This strain field $\varepsilon_x + \varepsilon_y$ is generated only by a pure compression wave (*i.e.* a longitudinal wave).

On the other hand, the radial displacement is expressed as a function of u_x and u_y as follows:

$$u_r = u_x cos\theta + u_y \sin\theta \tag{22}$$

Comparing Eqs. 21 and 22, it can be seen that for a longitudinal wave specified by Eq. 20, the expression for the radial displacement u_r is proportional to the strain field $\varepsilon_x + \varepsilon_y$. If the proportionality between the two quantities can be demonstrated with the numerical output data, then the second assumption would be validated, *viz.* radial displacements computed from the output data do correspond to motion induced by the scattered longitudinal waves and can therefore be used for the imaging. Furthermore, the first strain invariant could be used as well for the imaging and would produce similar reconstruction of the defect to those obtained in the following sections.

For this comparison between the strain invariant and the radial displacement, 12 sensors are selected to capture the scattered longitudinal waves, 6 for the transmitted wave and 6 for the reflected wave, which covers an angular aperture of 30° as shown in Fig. 6. This is done successively for a horizontal crack and a crack tilted by 25°. Radial displacements are easily computed from scattered displacements u_x and u_y but strains values are not provided as an output of the FE code. Therefore, they need to be computed with a independent post-processing procedure. Thus, 8 additional nodes are considered around each of the 12 sensors X_i to define a 3-by-3 nodes grid, as shown in Fig. 6. The scattered displacements u_x and u_y are recorded for each of the 9 nodes of the grid and strains are computed for each X_i using a second order finite differentiation. Note that the displacements have to be previously interpolated at each time step on a regular grid before computing the strains since the FE mesh is non-regular. The obtained strains are summed and then are compared to the radial displacement.

Fig. 7 shows a time signal example of the first strain invariant and the radial displacement for an output node located at (0 mm,-25 mm) in case of an horizontal crack. The scattered longitudinal wave is considered and the signals are normalized by their respective maximum of amplitude. This example shows a good proportionality between the two quantities, with a coefficient of correlation of 0.92. Table 1 gives the coefficient of correlation of the two signals for the 12 selected sensors, both for a horizontal crack and a tilted crack. The coefficients of correlation are close to 1 for all cases, which demonstrates the proportionality between the two signals. The signal arriving around 18 us in Fig. 7 can be attributed to internal crack

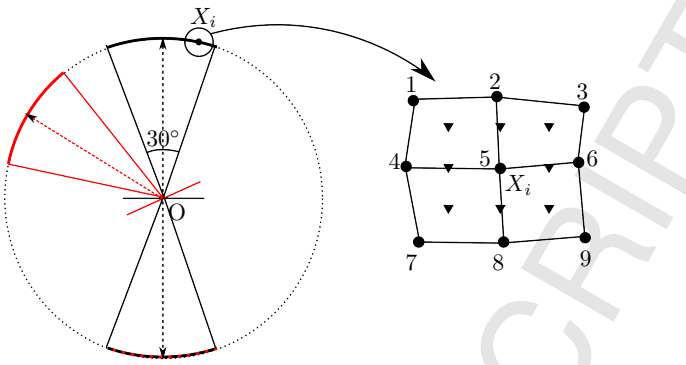

Figure 6: Definition of the reception arcs for strain and radial displacement computation, for a horizontal crack (black) and a crack tilted by 25° (red). Selection of a 3×3 node grid (black circle) around receiver X_i to compute the strains and the radial displacements. Displacements are interpolated on the inside regular grid (black triangle) to compute the strains.

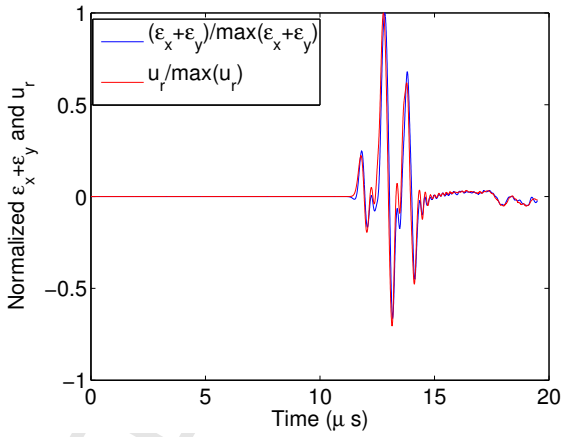

Figure 7: First strain invariant $\varepsilon_x + \varepsilon_y$ and radial displacement u_r generated at the position (0 mm,-25 mm) by the longitudinal wave scattered by a horizontal crack. Strains and displacements are normalized by their respective maximum amplitude.

dynamics, whereby diffraction of the incident pulse generates Rayleigh waves emanating from each crack tip and travelling towards the other tip. On arrival at the other tip, these Rayleigh waves are themselves diffracted, generating bulk waves, after a time delay corresponding to the Rayleigh wave travel time across the crack. These later contributions are removed from the radial displacement signals by time gating for the purposes of imaging.

The preceding results confirm that the longitudinal scattered wave can be separated from the shear waves in the time domain. Furthermore, the radial displacement and the first strain invariant computed from the numerical results are close, which confirms that radial displacement can be used for the imaging based on the scattered longitudinal waves in this numerical work. Note that the first strain invariant would be preferred if

$\alpha = 0°$	0.89	0.89	0.91	0.93	0.94	0.95	0.90	0.91	0.92	0.93	0.94	0.95
$\alpha = 25°$	0.98	0.98	0.98	0.98	0.99	0.99	0.92	0.92	0.93	0.94	0.95	0.96

Table 1: Coefficients of correlation between the radial displacement and the first strain invariant for two crack orientations considering 30° coverage of the forward and backward scattered waves with 12 sensors.

one considers potential application with Lamb waves since this quantity is actually measured by conventional piezoelectric sensors [83]. However, strain computation introduces additional steps in a numerical approach and requires additional data storage. For these reasons, radial displacements are selected in this work. The next section presents the imaging results for different cases.

5. Results and discussion

5.1. Closed crack imaging from fundamental and second harmonic scattering

The FE model and the MTR imaging algorithm are used to reconstruct the defect image based on the longitudinal wave scattering, using either the fundamental frequency or the second harmonic. The corresponding images are referred to as "fundamental harmonic image" and "second harmonic image". Fig. 8(a) shows the fundamental harmonic image of the closed crack where a pre-stress $\sigma_0 = -0.3$ MPa and a coefficient of friction $\mu = 0.3$ are considered. The crack is marked by the white dashed line and one can see that the main peak of the reconstructed image matches clearly the actual defect. Side-lobe peaks of decreasing amplitude are observed parallel to the crack. Fig. 8(b) gives the profiles of the reconstructed image respectively for $y = 0$ mm and then $x = 0$ mm. Following [34], a pragmatic approach for estimating the crack size in the reconstructed image is to consider the spacing between the half-amplitude points along the $y = 0$ mm profile. This procedure is illustrated in the top half of Fig. 8(b). The result in the present case is a crack length of 9.8 mm, which agrees closely with the actual crack length of 10 mm.

The profile at $x = 0$ mm shown in Fig. 8(b) is plotted together with the function $|\pi/(2k)J_0^2(ky)|$, where J_0 is the Bessel function of the first kind and $k = 2\pi\omega_1$. This function is the so-called point spread function (PSF), which gives the reconstructed image profile of a point scatterer obtained using the considered imaging algorithm [10]. It can be seen that the spacing of the side-lobes agrees quite well between the two curves. The interpretation of this result is that the image for a crack is like that for point scatterers smeared along a line segment, so that the side-lobes add up and appear as sidebands parallel to the crack.

The MTR algorithm is now used to construct the second harmonic image of the closed crack. The contact parameters are not modified and the reconstructed image is shown in Fig. 9(a). The reconstructed defect shows a main peak centered at the origin and two secondary peaks near the crack tips. The profile at $y = 0$ mm and $x = 0$ mm are plotted in Fig. 9(b). The crack size is still accurately estimated at half of the maximum amplitude. The side-lobes again follow the $|\pi/(2k)J_0^2(ky)|$ function where $k = 2\pi\omega_2$, although the

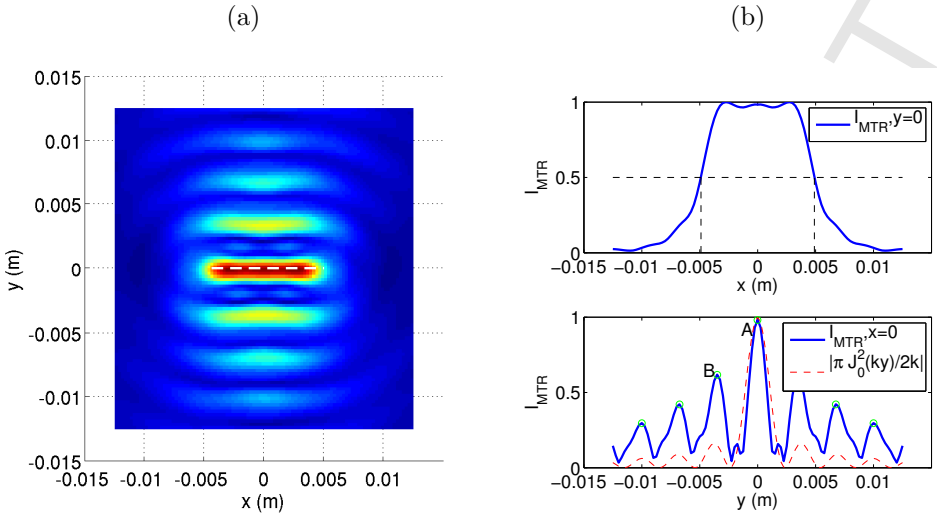

Figure 8: (a) fundamental harmonic image of the closed crack for 74 sensors and the following contact parameters: $\sigma_0 = -0.3$ MPa and $\mu = 0.3$. (b) profiles of the reconstructed image at $y = 0$ mm and $x = 0$ mm.

agreement is less accurate in this case. Nevertheless, the main lobe matches the theoretical profile, which is the most important feature of the PSF for imaging performance [10].

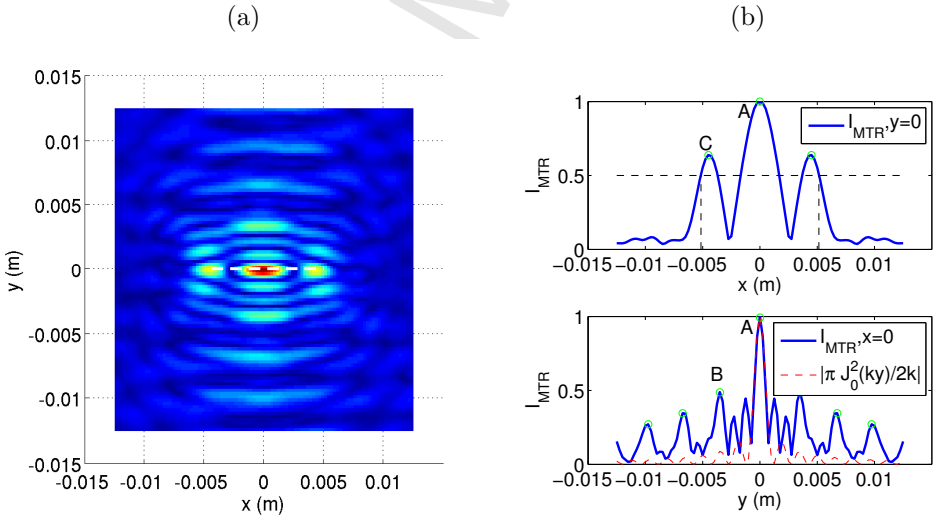

Figure 9: (a) second harmonic image of the closed crack for 74 sensors and the following contact parameters: $\sigma_0 = -0.3$ MPa and $\mu = 0.3$. (b) profiles of the reconstructed image at $y = 0$ mm and $x = 0$ mm.

The use of the second harmonic for the imaging offers a potential for a baseline free method for detection and characterization of closed cracks, because the second harmonic is only generated by the nonlinear interaction with the crack and is not present in the incident wave. Thus, the extraction of the second

harmonic from the scattered field $\hat{\boldsymbol{u}}(X_j, X_i, 2\omega_1) = \hat{\boldsymbol{u}}_T(X_j, X_i, 2\omega_1) - \hat{\boldsymbol{u}}_B(X_j, X_i, 2\omega_1)$ after the baseline subtraction is not required. The scattered amplitude of the second harmonic can actually be extracted directly from the total field as $\hat{\boldsymbol{u}}_T(X_j, X_i, 2\omega_1)$. Fig. 10 shows an example resulting from this approach for the contact parameter $\sigma_0 = -0.3$ MPa and $\mu = 0.3$. it can be seen that the image reconstructed from the second harmonic without performing a baseline subtraction is identical to the one obtained previously in Fig. 9. However, whereas this works quite well in the case of this numerical work where the level of second harmonic contained in the incident wave is only due to the finite duration of the excitation and therefore is negligible, strategies should be developed to take into account the effect of electronic and material nonlinearity that also generates second harmonic in the incident wave in practical application. Alternatively, it could be interesting to apply the MTR imaging method to side-band frequency components generated in case of nonlinear wave modulation.

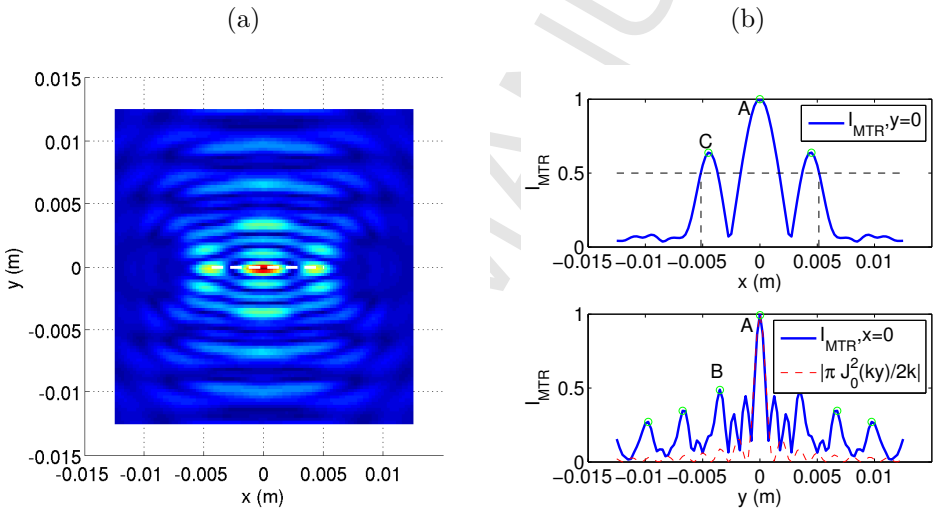

Figure 10: (a) second harmonic baseline free image of the closed crack for 74 sensors and the following contact parameters: $\sigma_0 = -0.3$ MPa and $\mu = 0.3$. (b) profiles of the reconstructed image at $y = 0$ mm and $x = 0$ mm.

The MTR imaging algorithm reconstructs the source of the wave scattering. Considering possible experimental application, the method would allow one to perform an *in-situ* imaging of the defect. Therefore, the external laser vibrometer scanning of the sample done in previous time reversal applications [36–47] to detect the re-focusing of the second harmonic would not be necessary. Fig. 9 and Fig. 10 indicate that the second harmonic is not equally generated along the crack unlike the fundamental in Fig. 8, but preferentially generated at the center of the crack and near the crack tips. It is noted that the three peaks profile oberved in the present second harmonic images are obtained for a 10 mm long crack. This result may not hold for other geometries and further work is required to establish whether the image obtained for longer cracks will also show three peaks, or whether the central peak may split into two or more peaks depending on the

crack length relative to the wavelength. Furthermore, it is known that compressive load applied to a contact interface directly impacts the reflection and transmission coefficients, as well as the generation of second harmonic [84]. The effect of static load is investigated in the next section.

5.2. Influence of contact parameters

The objective in this section is to assess the influence of the pre-stress parameter σ_0 on the reconstructed images. In particular, it is of interest to compare the fundamental harmonic image for no pre-stress ($\sigma_0 =$ 0 MPa) with the "linear" image, which is defined to be the reconstructed image in the absence of contact between the crack faces. More precisely, the contact laws are deactivated, so that the two faces of the crack do not interact. This corresponds to an open crack, like a slit, where the gap is just larger than the incident wave amplitude (a few nm), thereby removing CAN whilst maintaining the linear scattering response since the geometrical differences are negligible.

The linear image is shown in Fig. 11(a) and the two profiles at $y = 0$ mm and $x = 0$ mm are shown in Fig. 11(b) together with the corresponding profiles for the fundamental harmonic image with no pre-stress at the crack ($\sigma_0 = 0$ MPa). By comparing the profiles, it can be seen that the image obtained from the linear scattering is almost identical to the image obtained from the fundamental harmonic with no pre-stress. Crack face contact does occur in the latter case, resulting in a non-zero second harmonic scattered field which leads to a reconstructed image similar to that shown in Fig. 9. Thus, it seems that the introduction of contact does not appreciably change the scattering behavior of the fundamental harmonic. However, the curves presented in Fig. 11(b) are normalized and do not show the possible difference of amplitude of the reconstructed peaks.

Table 2 gives the raw amplitude (before normalization) of the main peak of the linear image on one hand, and the raw amplitude of the main peak of the fundamental and second harmonic images on the other hand. Including contact actually modifies the scattering of the fundamental harmonic by reducing substantially its amplitude although the profiles of the linear image and the fundamental harmonic image are similar. As expected, the introduction of contact generates second harmonic, but the amplitude of the reconstructed peak in the second harmonic image is almost two orders of magnitude smaller than the amplitude of the main peak in the fundamental harmonic image. Thus the introduction of contact does modify the scattering of the longitudinal wave. Considering the crack only, contact allows energy to be transfered through the interface, contrary to pure reflection in the case of an open crack. This leads to a reduction of the amplitude of the scattered waves. Nonlinear effects are small so that they do not change radically the motion of the crack faces. This explains why the reconstructed profiles for the linear image and the fundamental harmonic image with $\sigma_0 = 0$ MPa are not fundamentally different.

Scattering by the crack and harmonic generation are directly impacted by the stress state at the crack interface [84]. In the following, CAN is considered and the defects are reconstructed for several values of

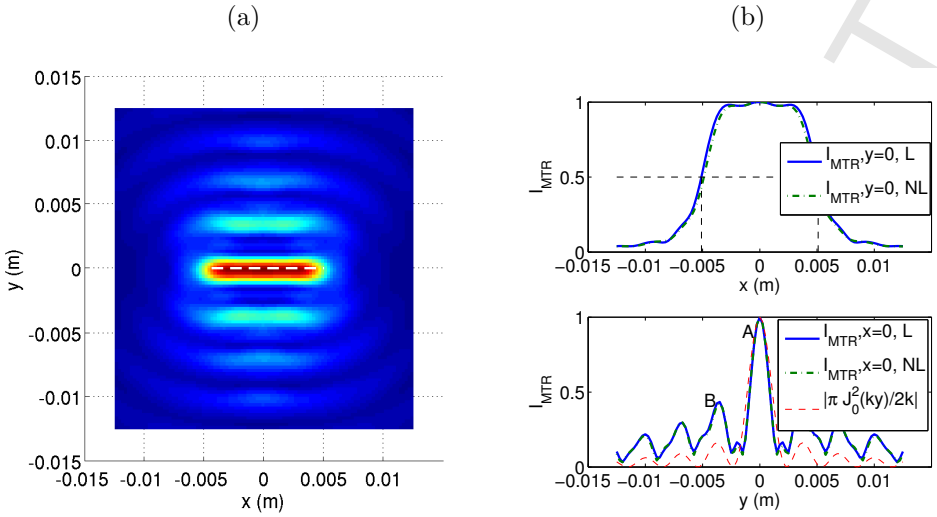

Figure 11: (a) reconstruction of the crack from the scattered longitudinal waves in the case of a linear interaction (no contact) between the incident waves and the crack using 74 sensors. (b) profiles of the reconstructed image at $y = 0$ mm and $x = 0$ mm for linear image (L) as well as for the fundamental harmonic image obtained for a pre-stress $\sigma_0 = 0$ MPa and a coefficient of friction $\mu = 0.3$ (NL).

	Linear image	Nonlinear image	
		Fundamental harmonic	Second harmonic
Raw amp. (a.u.)	7.86e-9	3.73e-9	6e-11

Table 2: Amplitude of the main peak for the linear image, the fundamental harmonic image and the second harmonic image.

the applied compressive stress σ_0, with $\sigma_0 \in [-0.5, -0.3, -0.1, 0]$ MPa and a coefficient of friction of 0.3. The following three quantities are extracted for examining the properties of the reconstructed image: (i) the crack length estimation, both for the fundamental and the second harmonic images; (ii) the ratio between the main peak and the first side-lobe, respectively identified by A and B in Fig. 8(b) for the fundamental harmonic image and in Fig. 9(b) for the second harmonic image; (iii) the ratio between the main peak and the secondary peak at the crack tips in the case of the second harmonic image. These peaks are identified by A and C in Fig. 9(b).

Fig. 12(a) and (b) shows respectively the evolution of the error made on the crack length estimation and the ratio of the different peaks as a function of the applied load. For the images based on the fundamental harmonic, the crack length estimation obtained from half the maximum amplitude at $y = 0$ mm are excellent, with a maximum error of -2.5% for $\sigma_0 = 0$ MPa. The crack length estimation based on the second harmonic are correct for intermediate load levels, with an error up to 13% at $\sigma_0 = -0.5$ MPa. However the estimation

fails in the case of a stress-free crack because the reconstruction includes additional peaks of high amplitude around the crack tips.

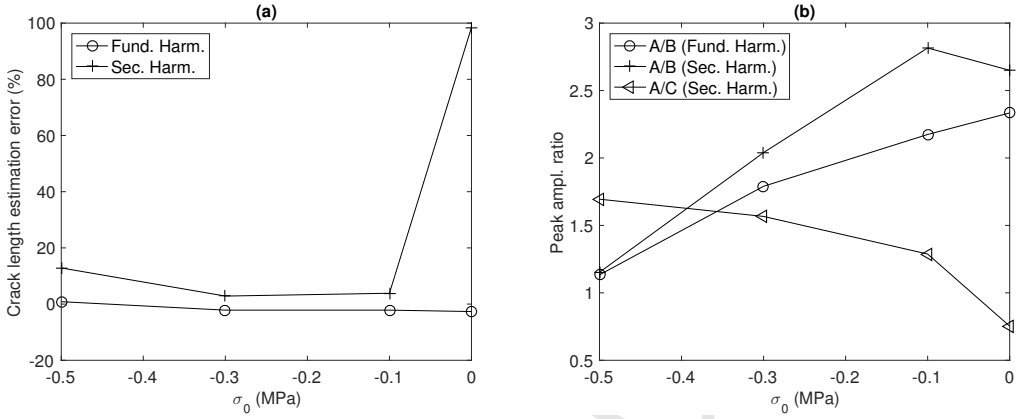

Figure 12: Effect of the applied pre-stress on the crack on (a) the relative percentage error in the estimation of crack length, based on the fundamental and second harmonic images and (b) the amplitude ratio between the main peak and the first side-lobe (A/B) for the fundamental and second harmonic images and between the main peak and the secondary peak (A/C) for the second harmonic image.

Regarding the side-lobes along the $\boldsymbol{y}$ direction, Fig. 12(b) shows that their amplitude increases as the pre-stress becomes stronger for both the fundamental and second harmonic images. For $\sigma_0 = -0.5$ MPa, the amplitude of the main peak and the first pair of side-lobe are almost equal at $x = 0$ mm. Therefore, as the load increases, it becomes more delicate to identify the defect as the peak of highest amplitude. Note that away from the axis $x = 0$ mm, the difference between the main peak and the side-lobes remains important. It has been demonstrated that the compression decreases the scattering of the fundamental harmonic [84]. For $\sigma_0 = -0.5$ MPa the crack is still temporarily open during the interaction with the incident wave, since the maximum stress σ_{yy} generated the incident wave is 1 MPa, but the amplitude of the scattered wave is too weak to obtain a clear reconstruction of the defect. As the compressive load increases, the crack becomes a weak scatterer and the MTR algorithm is found to under-perform. It is noted that the present results are obtained for scattered field data at a single input frequency. It is possible that better lateral resolution may be obtained by averaging the image over a finite frequency bandwidth. Such averaging has been found to sometimes improve the image quality for linear imaging [35, 74], depending on the actual bandwidth that is employed, and this strategy should be further investigated in future work.

The same result is observed for the second harmonic images when the compression is equal to -0.5 MPa. By contrast, the reduction of the compressive stress enhances the secondary peaks near the cracks tips, which get greater than the central peak for $\sigma_0 = 0$ MPa. As the pre-stress gets smaller, the crack tends to open freely at the center and contact-induced second harmonic tend to be preferentially generated near the crack

tips. To demonstrate that the increase of the secondary peaks amplitude is linked to a modification of the second harmonic generation along the contact interface, the FFT is applied to the time history of the nodal displacements along the crack, in the case of an incident wave propagating along the normal direction to the crack. This provides the values of the fundamental and second harmonics directly generated along the crack, as shown in Fig. 13(a) and (b) for pre-stress $\sigma_0 = -0.3$ MPa and $\sigma_0 = 0$ MPa respectively. It can be seen that when no compressive stress is applied, there is a higher relative level of second harmonic near the crack tips. This correlates with the second harmonic images, and the increase of peak amplitudes near the crack tips.

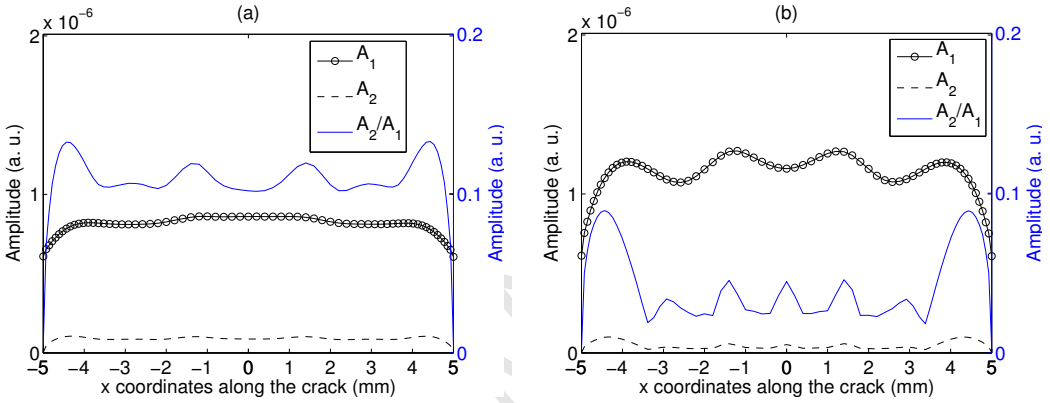

Figure 13: Evolution of the first and second harmonic as well as their ratio along the crack for a normal incidence and for a pre-stress of (a) $\sigma_0 = -0.3$ MPa and (b) $\sigma_0 = 0$ MPa. The coefficient of friction is 0.3.

The MTR algorithm performs well for low compressive stress levels, but when the load increases the crack becomes a weak scatterer and this algorithm is then of limited efficiency whatever harmonic is used. Nevertheless, the main peak of the image provides a very good estimation of the crack location and size. In case of larger compression stress, other methods better suited for weak scatterer, such as the Diffraction Tomography, could provide a better result. Finally, it was found that varying the coefficient of friction had a negligible influence in this case, where longitudinal wave are considered for the incident and scattered waves.

5.3. Influence of the number of sensors

The imaging algorithm used in this work supposes that the number of sensors N is sufficient to fulfill the Nyquist sampling criterion with respect to the imaging domain dimensions. Therefore, considering a 25×25 mm^2 imaging domain and a wavelength $\lambda_2 \simeq 3$ mm for the second harmonic, the number of sensors was set to 74. This relatively large number needs to be reduced for practical application of the method. In this section, the quality of the defect reconstruction is evaluated as the number of sensors is reduced. However, following the approach proposed in [35], a re-sampling of the multi-static $\boldsymbol{K}$ matrix is performed

to maintain 74×74 cells, thus ensuring that the Nyquist criterion is still observed. The re-sampling is done using the cubic smoothing spline Matlab interpolation function (csaps).

Fig. 14(a) and (b) show respectively the fundamental and the second harmonic images of the defect using 38 equi-spaced sensors, with the same contact conditions as in Fig. 8 and Fig. 9. The image reconstructed from the fundamental harmonic using 38 sensors is identical as the image obtained previously for 74 sensors. The image generated from the second harmonic is again similar to the one obtained with 74 sensors, with the difference that the secondary peaks near the crack tips are slightly enhanced.

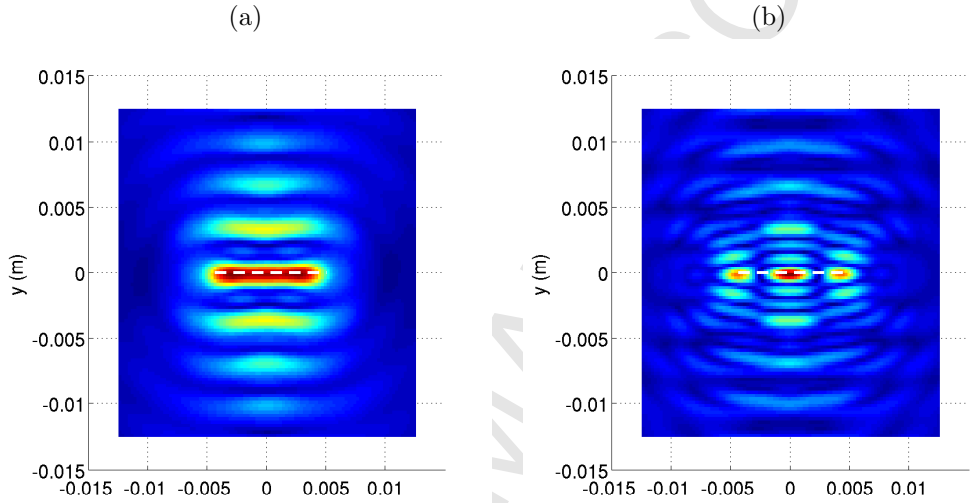

Figure 14: (a) fundamental and (b) second harmonic reconstruction image of the closed crack for 38 sensors and the following contact parameters: $\sigma_0 = -0.3$ MPa and $\mu = 0.3$.

The two profiles of the reconstructed images are analyzed as done previously, to estimate the crack length and to evaluate the ratio between the main peak and the side-lobes or the secondary peaks in the case of the nonlinear image. Fig. 15(a) and (b) show the evolution of the error made on the crack length estimation and the ratio between the different peaks as a function of the number of sensors. It can be seen that the characteristics of the fundamental harmonic image are almost constant when at least 20 sensors are used, with still a good crack length estimation when only 10 sensors are used, provided that the up-sampling procedure is applied. The image reconstructed from the second harmonic is more sensitive to the number of sensors, and the amplitude of the secondary peaks near the crack tips varies when the number of sensors is less than 40. Above this number, the characteristics of the image are consistent.

This requirement of a higher number of sensors can be attributer to a more directional scattering of the second harmonic due to a shorter wavelength. The enhancement of the directivity of the second harmonic is demonstrated by comparing the $\boldsymbol{K}$ matrix obtained from the fundamental and the second harmonic. Fig. 16 (a) and (b) show the density plots of the absolute value of the $\boldsymbol{K}$ matrix obtained from the fundamental and

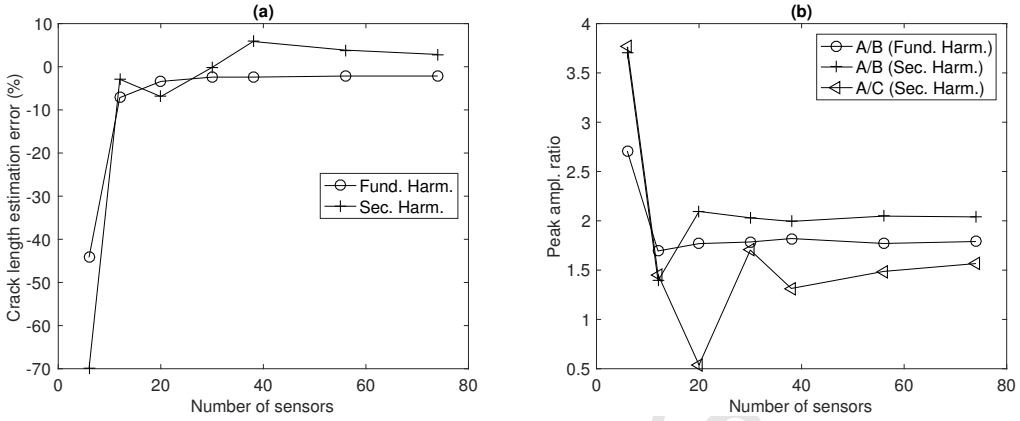

Figure 15: Effect of the number of sensors on (a) the estimation of the crack length, based on the fundamental and second harmonic images and (b) the amplitude ratio between the main peak and the first side-lobe (A/B) for the fundamental and second harmonic images and between the main peak and the secondary peak (A/C) for the second harmonic image.

the second harmonic respectively, where each pixel corresponds to the absolute amplitude of the scattered field at the frequency $\omega_{1,2}$ for each emitter-receiver pair (X_j, X_i). By plotting the amplitude of the $\boldsymbol{K}$ matrix, one can know which sensors are preferentially receiving the scattered waves for each actuator. It can be seen that in the case of the second harmonic (Fig. 16(b)), the peaks of amplitude are much narrower than in the case of the fundamental harmonic (Fig. 16(a)). For a given actuator, only a few sensors receive scattered signals containing the second harmonic, which indicate a more directional scattering. Thus, using equi-spaced sensors, a larger number is required to ensure an adequate sampling of the second harmonic scattered field.

5.4. Multi-frequency imaging

The preceding results are based on the single-frequency algorithms given by Eqs. 15 (a, b). This is a conventional and frequently used approach for diffraction tomography and related imaging algorithms [10, 15–18, 74–76]. However, the input tone burst has a finite bandwidth, so that scattered field data is available over a frequency band, rather than just a single frequency. The algorithms in Eqs. 15 (a, b) can be readily extended to make use of this data simply by integrating the reconstructed image over the available bandwidth. Such multi-frequency reconstructions have been previously explored for Lamb wave imaging [35, 74], but this did not always result in improved image quality. The objective in this section is to examine the imaging performance of multi-frequency (finite bandwidth) imaging for both the fundamental and second harmonic imaging.

Figure 17 shows the frequency spectrum for the 5-cycle tone burst that is used in the present work, cf. Sec. 4.1. The half-amplitude bandwidth is indicated by dashed vertical lines as $\Delta f \simeq 400$ kHz. Fig. 17

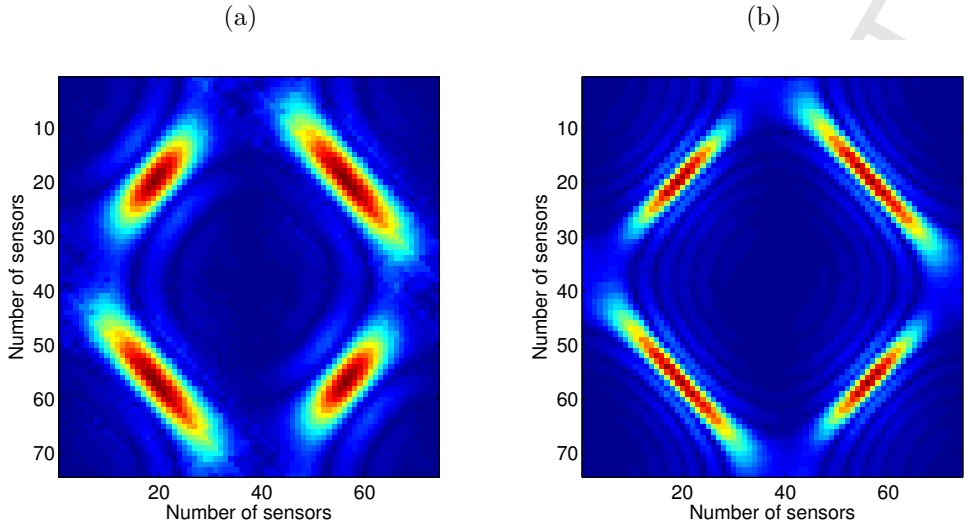

Figure 16: Density plots of the absolute value of multi-static $\boldsymbol{K}$ matrix for (a) the fundamental harmonic and (b) the second harmonic. The contact parameters are: $\sigma_0 = -0.3$ MPa and $\mu = 0.3$.

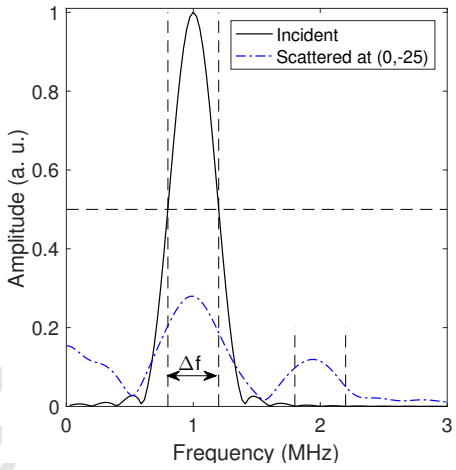

Figure 17: Spectrum of the incident wave and scattered longitudinal wave signals. Spectra are normalized by the incident wave spectrum maximal amplitude. The scattered wave displacements are recorded at (0 mm, -25 mm) in the case of an horizontal crack, with $\sigma_0 = -0.3$ MPa.

also displays the scattered field spectrum for a representative observation point at (0 mm, -25 mm), showing broad peaks around the fundamental (1 MHz) and second harmonic (2 MHz) frequencies. To construct a multi-frequency fundamental image, Eq. 15(a) is integrated over the bandwidth Δf around 1 MHz, as indicated in Fig. 17, and the image is normalized in accordance with Eq. 16. Similarly, a multi-frequency second harmonic image is constructed by integrating Eq. 15(b) over a frequency band of the same width

Δf around 2 MHz, which is also indicated by dashed vertical lines in Fig. 17. In both cases, data from 74 sensors is used to ensure adequate sampling.

Figures 18 (a) and (b) show respectively the single frequency image and the multi-frequency image corresponding to the fundamental harmonic, for a representative example with contact parameters $\sigma_0 = -0.1$ MPa and $\mu = 0.3$. Fig. 19 (a) and (b) show the results for the single and multi-frequency image for the second harmonic, under the same conditions. For the example of the fundamental harmonic, the multi-frequency imaging results in a 50% increase of the ratio between the main peak amplitude A and the second highest peak amplitude B along the $\boldsymbol{y}$ axis as defined in Fig. 8, in comparison with the single frequency image. The signal-to-noise ratio is thus improved, while the lateral definition of the image along $\boldsymbol{x}$ is marginally altered, with a crack length estimation dropping from 9.8 mm to 9.7 mm. For the second harmonic case however, the A/B ratio actually decreases by 5% when considering the multi-frequency data, which means that the quality if the image slightly decreases. The crack length estimation is not modified in this case.

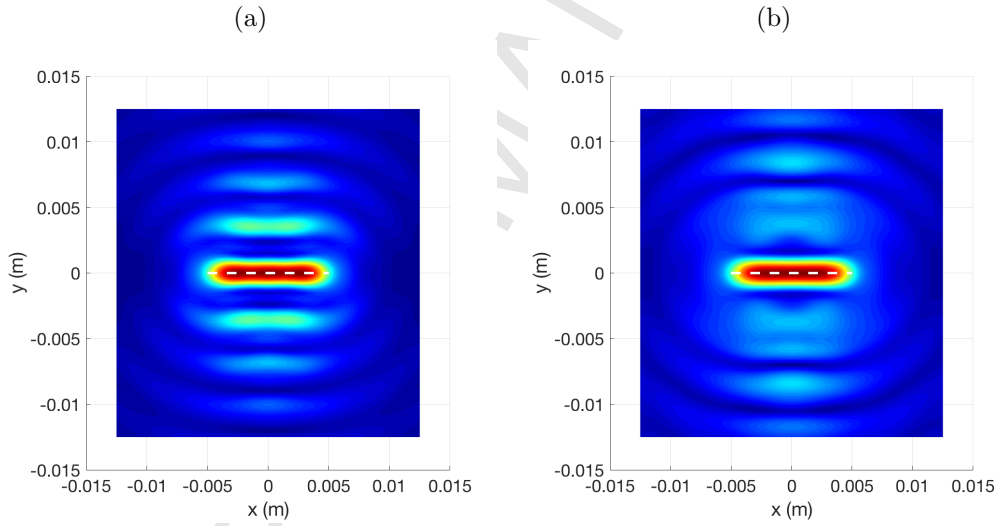

Figure 18: Fundamental harmonic reconstruction image of the closed crack using (a) a single frequency data and (b) a multi-frequency data, for 74 sensors and the following contact parameters: $\sigma_0 = -0.1$ MPa and $\mu = 0.3$.

The above results showed that taking into account the frequency bandwidth information may improve the image quality, mainly as regard the signal-to-noise ratio. But the improvement is not systematic depending on the considered harmonic and comes with potential reduction in accuracy regarding the crack length estimation. However, these results are given for a specific load case and sensors configuration. For completeness, the crack length estimation and the peak amplitude ratio A/B and A/C, as defined in Fig. 9, are shown in Fig. 20 for different loads and in Fig. 21 for different number of sensors. The results obtained with the multi-frequency approach correspond to the red dashed curves, whereas the previous results shown

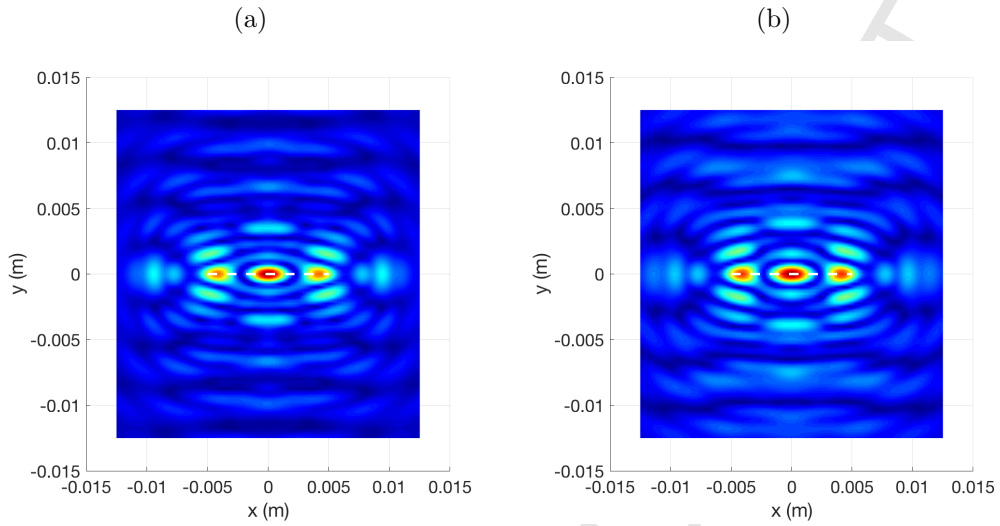

Figure 19: Second harmonic reconstruction image of the closed crack using (a) a single frequency data and (b) a multi-frequency data, for 74 sensors and the following contact parameters: $\sigma_0 = -0.1$ MPa and $\mu = 0.3$.

in Fig. 12 and 15 for a single frequency imaging are plotted in solid black curves.

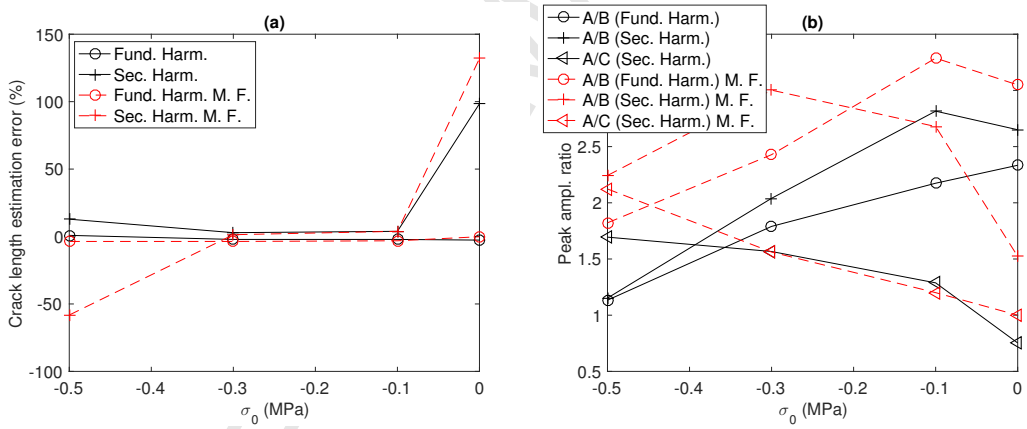

Figure 20: Comparison between single frequency imaging (solid black lines) and multiple frequency (M. F.) imaging (dashed red lines) regarding the effect of the number of sensors on (a) the estimation of the crack length, based on the fundamental and second harmonic images and (b) the amplitude ratio between the main peak and the first side-lobe (A/B) for the fundamental and second harmonic images and between the main peak and the secondary peak (A/C) for the second harmonic image.

The multi-frequency imaging improves the signal-to-noise ratio (A/B) for the fundamental harmonic images over the whole load range and provides similar crack length estimations as the single frequency approach. However, this is not true for the second harmonic images, especially for low load levels, where the side-lobe ratio (A/B) is lower than the one obtained with the single frequency imaging. For the second

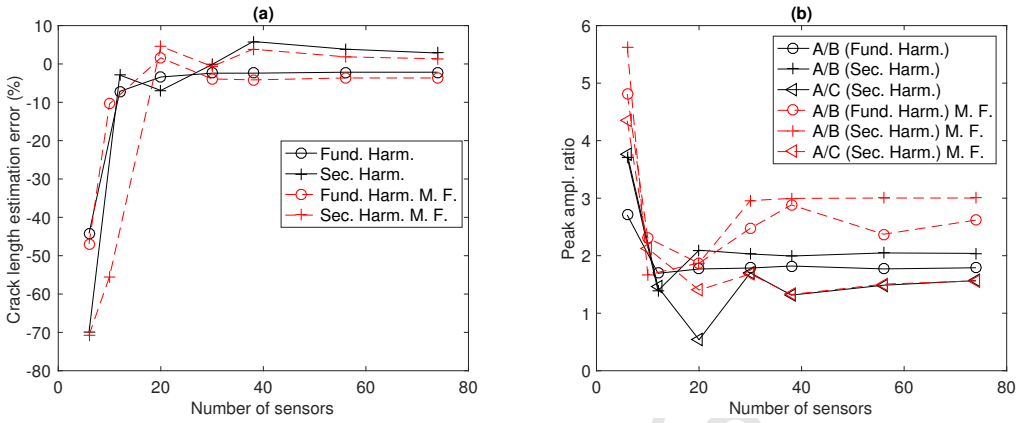

Figure 21: Comparison between single frequency imaging (solid black lines) and multiple frequency (M. F.) imaging (dashed red lines) regarding the effect of the number of sensors on (a) the estimation of the crack length, based on the fundamental and second harmonic images and (b) the amplitude ratio between the main peak and the first side-lobe (A/B) for the fundamental and second harmonic images and between the main peak and the secondary peak (A/C) for the second harmonic image.

harmonic, the secondary peak ratio (A/C) at $\sigma_0 = -0.5$ MPa is larger when using the multi-frequency approach, which leads to a largely increased error in crack length estimation in that case.

Regarding the effect of the number of sensors, side-lobe ratio (A/B) is better when using the multi-frequency approach, provided that at least 30 sensors are used. In that case, the crack length estimation are slightly worse for the fundamental harmonic and slightly better of the second harmonic. For a small number of sensors, the benefit of multi-frequency imaging is not sensible in terms of signal-to-noise ratio and more importantly the crack length estimations based on the second harmonic degrade compared with the single frequency imaging.

The multi-frequency imaging approach may improve the robustness of the imaging algorithm when using the fundamental harmonic, but care must be taken when considering the second harmonic. The choice of the bandwidth window may also have an influence on the results and should be investigated.

6. Conclusion

It is recognized that closed cracks are difficult to detect due to their weaker scattering relative to fully open cracks. By contrast CAN may be activated at a closed crack, which generates higher harmonics. In this work, linear and nonlinear scattering responses generated by the propagation of incident plane longitudinal waves have been used to reconstruct images of the crack through the Modified Time Reversal imaging algorithm.

It has been shown that a clear image of the defect can be reconstructed from the scattering of the

fundamental harmonic, giving an excellent estimation of the crack length. The present work is also the first time that the second harmonic component of the nonlinear scattered field has been used (in conjunction with a rigorous imaging algorithm and the correct theoretical sampling requirement) to reconstruct an *in-situ* image of a realistic defect. This nonlinear image can be used for two purposes. First it enables to detect the crack and estimate its size as well as the classical imaging based on the fundamental harmonic but without requiring external scanning of the sample. The fundamental and second harmonic images are quite different, since the first one shows one main peak centered on the crack whereas the second one shows generally three peaks, one centered on the crack and two around the crack tips. It has been shown that these peaks identify the locations of the source of the second harmonic. Therefore, the nonlinear imaging can bring some benefit in the understanding of the harmonic generation due to CAN. Second, this offers potential application for baseline-free imaging because of the second harmonic in the signal can be attributed to CAN. Finally, the use of both the fundamental and second harmonic can be done simultaneously to take advantage of the two images and improve the characterization of closed cracks.

One of the main parameters influencing the scattering and the generation of higher harmonic by a closed crack is the applied compressive load. When the load increases, the crack closes and becomes a weak scatterer and the quality of the images degrades, both from fundamental and second harmonic. However, the crack length estimation is still good when considering the main peak of the reconstructed image. Investigating other imaging methods best suited for weak scatterer may be of interest in a future work. For low level of compressive load, the crack tips are highlighted by the nonlinear image. The level of CAN can be closely controlled in the FE model by varying the compressive pre-stress. This forward modeling should prove valuable for implementing and interpreting inverse modeling of CAN for practical cases of structural damage, such as plasticity-induced fatigue crack closure [58, 59]. The requirement regarding the number of sensors can be overcome if the multi-static matrix is re-sampled. It has been shown that 10 sensors are enough for the imaging based on the fundamental harmonic. The imaging based on the second harmonic still requires a higher number of equally spaced sensors because of the shorter wavelength and the higher directivity of the scattered second harmonic. Finally, a multi-frequency imaging approach has been considered to include information over a finite bandwidth representative of the employed tone-burst. The obtained results are compared with the single frequency imaging results and it is shown that while multi-frequency imaging provides some improvement for the fundamental harmonic imaging, there does not appear to be an improvement for second harmonic imaging.

Acknowledgment

This study was supported in part by an Australian Research Council (ARC) Discovery Grant (DP150101899).

Bibliography

[1] I. Y. Solodov, Ultrasonics of non-linear contacts: propagation, reflection and NDE-applications, Ultrasonics 36 (1998) 383–390.

[2] K. Van Den Abeele, P. A. Johnson, A. Sutin, Nonlinear Elastic Wave Spectroscopy (NEWS) Techniques to Discern Material Damage, Part I: Nonlinear Wave Modulation Spectroscopy (NWMS), Journal of Nondestructive Evaluation 12 (2000) 17–30.

[3] D. Donskoy, A. Sutin, A. Ekimov, Nonlinear Acoustic interaction on contact surfaces and its use for nondestructive testing, NDT & E International 34 (2001) 231–238.

[4] I. Y. Solodov, N. Krohn, G. Busse, CAN: an example of nonclassical acoustic nonlinearity in solids, Ultrasonics 40 (2002) 621–625.

[5] I. Y. Solodov, J. Wackerl, K. Pfleiderer, G. Busse, Nonlinear self-modulation and subharmonic acoustic spectroscopy for damage detection and location, Applied Physics Letters 84 (26) (2004) 5386–5388.

[6] P. B. Nagy, Fatigue damage assessment by nonlinear ultrasonic materials characterization, Ultrasonics 36 (1998) 375–381.

[7] Y. Zheng, R. G. Maev, I. Y. Solodov, Nonlinear acoustic applications for material characterization: a review, Canadian Journal of Physics 77 (1999) 927–967.

[8] C. Pruell, J.-Y. Kim, J. Qu, L. J. Jacobs, Evaluation of fatigue damage using nonlinear guided waves, Smart Materials and Structures 18 (3) (2009) 35003.

[9] K.-Y. Jhang, Nonlinear Ultrasonic Techniques for Nondestructive Assessment of Micro Damage in Material: A Review, International Journal of Precision Engineering and Manufacturing 10 (1) (2009) 123–135.

[10] L. R. F. Rose, E. Chan, C. H. Wang, A comparison and extensions of algorithms for quantitative imaging of laminar damage in plates. I. Point spread functions and near field imaging, Wave Motion 58 (2015) 222–243.

[11] E. Chan, L. R. F. Rose, C. H. Wang, A comparison and extensions of algorithms for quantitative imaging of laminar damage in plates. II. Non-monopole scattering and noise, Wave Motion In Press.

[12] P. Blanloeuil, A. Meziane, C. Bacon, Nonlinear interaction of ultrasonic waves with a crack of different orientations, AIP Conference Proceedings 1511 (1) (2013) 99–106.

[13] P. Blanloeuil, A. Meziane, A. N. Norris, M. Renier, M. Veidt, Numerical Computation of the Nonlinear Far Field of Ultrasonic Waves Scattered by Closed Cracks of Various Orientations, in: EWSHM - 7th European Workshop on Structural Health Monitoring, 2014.

[14] P. Blanloeuil, A. Meziane, C. Bacon, Numerical study of nonlinear interaction between a crack and elastic waves under an oblique incidence, Wave Motion 51 (3) (2014) 425–437.

[15] A. C. Kak, M. Slaney, Principles of Computerized Tomographic Imaging, IEEE Press, New York, 1988.

[16] A. J. Devaney, M. Dennison, Inverse scattering in inhomogeneous background media, Inverse Problems 19 (4) (2003) 855.

[17] E. Chan, L. R. F. Rose, C. H. Wang, An extended diffraction tomography method for quantifying structural damage using numerical Green's functions, Ultrasonics 59 (2015) 1–13.

[18] A. J. Devaney, Mathematical Foundations of Imaging, Tomography and Wavefield Inversion, Cambridge University Press, 2012.

[19] C. H. Wang, J. T. Rose, F.-K. Chang, A synthetic time-reversal imaging method for structural health monitoring, Smart Materials and Structures 13 (2) (2004) 415.

[20] J. E. Michaels, Detection, localization and characterization of damage in plates with an in situ array of spatially distributed ultrasonic sensors, Smart Materials and Structures 17 (2008) 35035.

[21] F. Simonetti, L. Huang, From beamforming to diffraction tomography, Journal of Applied Physics 103 (10) (2008) 103110.

[22] S. J. Norton, M. Linzer, Ultrasonic reflectivity tomography: reconstruction with circular transducer arrays, Ultrasonic Imaging 1 (1979) 123–133.

[23] L. J. Busse, Three-dimensional imaging using a frequency-domain synthetic aperture focusing technique, Ultrasonics, Ferroelectrics, and Frequency Control, IEEE Transactions on 39 (2) (1992) 174–179.

[24] R. Sicard, J. Goyette, D. Zellouf, A SAFT algorithm for lamb wave imaging of isotropic plate-like structures, Ultrasonics 39 (7) (2002) 487–494.

[25] C. Holmes, B. W. Drinkwater, P. D. Wilcox, Post-processing of the full matrix of ultrasonic transmit-receive array data for non-destructive evaluation, NDT & E International 38 (8) (2005) 701–711.

[26] J. Zhang, B. W. Drinkwater, P. D. Wilcox, A. J. Hunter, Defect detection using ultrasonic arrays: The multi-mode total focusing method, NDT and E International 43 (2) (2010) 123–133.

[27] A. Velichko, P. D. Wilcox, An analytical comparison of ultrasonic array imaging algorithms., The Journal of the Acoustical Society of America 127 (March 2009) (2010) 2377–2384.

[28] W.-F. Chang, Reverse-time migration of offset vertical seismic profiling data using the excitation-time imaging condition, Geophysics 51 (1) (1986) 67.

[29] X. Lin, F. G. Yuan, Experimental Study Applying a Migration Technique in Structural Health Monitoring, Structural Health Monitoring 4 (4) (2005) 341–353.

[30] B. E. Anderson, M. Griffa, P.-y. L. Bas, T. J. Ulrich, P. A. Johnson, Experimental implementation of reverse time migration for nondestructive evaluation applications., The Journal of the Acoustical Society of America 129 (1) (2011) EL8–14.

[31] E. Kerbrat, C. Prada, D. Cassereau, M. Fink, Imaging in the presence of grain noise using the decomposition of the time reversal operator, The Journal of the Acoustical Society of America 113 (3) (2003) 1230–1240.

[32] A. J. Devaney, Time reversal imaging of obscured targets from multistatic data, Antennas and Propagation, IEEE Transactions on 53 (5) (2005) 1600–1610.

[33] E. Bavu, A. Berry, High-resolution imaging of sound sources in free field using a numerical time-reversal sink, Acta Acustica united with Acustica 95 (4) (2009) 595–606.

[34] C. H. Wang, L. R. F. Francis Rose, Imaging damage using mixed passive and active sensors, in: Key Engineering Materials, Vol. 558, Trans Tech Publ, 2013, pp. 244–251.

[35] E. Chan, L. R. F. Rose, C. H. Wang, Multi-frequency Approach to Imaging Damage in Stiffened Structures Exhibiting Multi-path Reflections, in: Structural Health Monitoring, 2015.

[36] T. Goursolle, S. Calle, S. D. Santos, O. B. Matar, A two-dimensional pseudospectral model for time reversal and nonlinear elastic wave spectroscopy, The Journal of the Acoustical Society of America 122 (6) (2007) 3220–3229.

[37] T. J. Ulrich, P. A. Johnson, A. Sutin, Imaging nonlinear scatterers applying the time reversal mirror, The Journal of the Acoustical Society of America 119 (3) (2006) 1514–1518.

[38] T. Goursolle, S. D. Santos, O. B. Matar, S. Callé, Non-linear based time reversal acoustic applied to crack detection: Simulations and experiments, International Journal of Non-Linear Mechanics 43 (3) (2008) 170–177.

[39] T. J. Ulrich, P. A. Johnson, R. A. Guyer, Interaction Dynamics of Elastic Waves with a Complex Nonlinear Scatterer through the Use of a Time Reversal Mirror, Physical Review Letters 98 (10) (2007) 104301.

[40] T. J. Ulrich, B. E. Anderson, M. C. Remillieux, P. Y. Le Bas, L. Pieczonka, Application of nonlinear ultrasonics to inspection of stainless steel for dry storage, Tech. rep. LA-UR-15-27382, Los Alamos National Laboratory (LANL) (2015).

[41] P. Y. Le Bas, M. C. Remillieux, L. Pieczonka, J. A. Ten Cate, B. E. Anderson, T. J. Ulrich, Damage imaging in a laminated composite plate using an air-coupled time reversal mirror, Applied Physics Letters 107 (18).

[42] P. Y. Le Bas, B. E. Anderson, M. C. Remillieux, L. Pieczonka, T. J. Ulrich, Characterizing defects with nonlinear acoustics, in: 170th ASA meeting, 2015.

[43] H. J. Lim, B. Song, B. Park, H. Sohn, Noncontact fatigue crack visualization using nonlinear ultrasonic modulation, NDT & E International 73 (2015) 8–14.

[44] P. Liu, H. Sohn, S. Yang, T. Kundu, Fatigue crack localization using noncontact laser ultrasonics and state space attractors, The Journal of the Acoustical Society of America 138 (2) (2015) 890–898.

[45] K. Kawashima, M. Murase, R. Yamada, M. Matsushima, M. Uematsu, F. Fujita, Nonlinear ultrasonic imaging of imperfectly bonded interfaces, Ultrasonics 44 (SUPPL.) (2006) 1329–1333.

[46] T. H. Lee, K. Y. Jhang, Experimental investigation of nonlinear acoustic effect at crack, NDT & E International 42 (2009) 757–764.

[47] J. Rivière, M. C. Remillieux, Y. Ohara, B. E. Anderson, S. Haupert, T. J. Ulrich, P. A. Johnson, Dynamic acousto-elasticity in a fatigue-cracked sample, Journal of Nondestructive Evaluation 33 (2) (2014) 216–225.

[48] Y. Nakagawa, W. Hou, A. Cai, N. Arnold, G. Wade, Nonlinear Parameter Imaging with Finite-Amplitude Sound Waves, in: IEEE 1986 Ultrasonics Symposium, 1986, pp. 901–904.

[49] A. Cai, J.-a. Sun, G. Wade, Imaging the acoustic nonlinear parameter with diffraction tomography, Ultrasonics, Ferroelectrics, and Frequency Control, IEEE Transactions on 39 (6) (1992) 708–715.

[50] D. Zhang, X.-f. Gong, X. Chen, Experimental imaging of the acoustic nonlinearity parameter B/A for biological tissues via a parametric array, Ultrasound in Medicine & Biology 27 (10) (2001) 1359–1365.

[51] S. L. Mulvagh, D. A. Foley, B. C. Aeschbacher, K. K. Klarich, J. B. Seward, Second harmonic imaging of an intravenously administered echocardiographic contrast agentVisualization of coronary arteries and

measurement of coronary blood flow, Journal of the American College of Cardiology 27 (6) (1996) 1519–1525.

[52] X. A. A. M. Verbeek, L. A. F. Ledoux, J. M. Willigers, P. J. Brands, A. P. G. Hoeks, Experimental investigation of the pulse inversion technique for imaging ultrasound contrast agents, Journal of the Acoustical Society of America 107 (4) (2000) 2281–2290.

[53] V. V. Kazakov, A. Sutin, P. A. Johnson, Sensitive imaging of an elastic nonlinear wave-scattering source in a solid, Applied Physics Letters 81 (4) (2002) 646–648.

[54] J. P. Jiao, B. W. Drinkwater, S. a. Neild, P. D. Wilcox, Low-frequency vibration modulation of guided waves to image nonlinear scatterers for structural health monitoring, Smart Materials and Structures 18 (6) (2009) 065006.

[55] M. Scalerandi, a. S. Gliozzi, C. L. E. Bruno, K. Van Den Abeele, Nonlinear acoustic time reversal imaging using the scaling subtraction method, Journal of Physics D: Applied Physics 41 (21) (2008) 215404.

[56] J. N. Potter, A. J. Croxford, P. D. Wilcox, Nonlinear ultrasonic phased array imaging, Physical Review Letters 113 (14) (2014) 1–5.

[57] Y. Ohara, S. Yamamoto, T. Mihara, K. Yamanaka, Ultrasonic evaluation of closed cracks using subharmonic phased array, Japanese Journal of Applied Physics 47 (5 PART 2) (2008) 3908–3915.

[58] Y. Ohara, T. Mihara, R. Sasaki, T. Ogata, S. Yamamoto, Y. Kishimoto, K. Yamanaka, Imaging of closed cracks using nonlinear response of elastic waves at subharmonic frequency, Applied Physics Letters 90 (1) (2007) 11902–119023.

[59] Y. Ohara, S. Horinouchi, M. Hashimoto, Y. Shintaku, K. Yamanaka, Nonlinear ultrasonic imaging method for closed cracks using subtraction of responses at different external loads, Ultrasonics 51 (6) (2011) 661–666.

[60] C.-S. Park, J.-W. Kim, S. Cho, D.-c. Seo, A high resolution approach for nonlinear sub-harmonic imaging, NDT & E International 79 (2016) 114–122.

[61] G. Zumpano, M. Meo, A new nonlinear elastic time reversal acoustic method for the identification and localisation of stress corrosion cracking in welded plate-like structures – A simulation study, International Journal of Solids and Structures 44 (11–12) (2007) 3666–3684.

[62] E. Barbieri, M. Meo, Time reversal DORT method applied to nonlinear elastic wave scattering, Wave Motion 47 (7) (2010) 452–467.

[63] F. Ciampa, M. Meo, Nonlinear elastic imaging using reciprocal time reversal and third order symmetry analysis, The Journal of the Acoustical Society of America 131 (6) (2012) 4316.

[64] F. Ciampa, G. Scarselli, S. Pickering, M. Meo, Nonlinear elastic wave tomography for the imaging of corrosion damage, Ultrasonics 62 (2015) 147–155.

[65] W. Li, Y. Cho, Combination of nonlinear ultrasonics and guided wave tomography for imaging the micro-defects, Ultrasonics 65 (2016) 87–95.

[66] L. R. F. Rose, C. H. Wang, A comparison of algorithms for in-situ imaging of structural damage, in: Proc. 6th Australian Congress On Applied Mechanics, Perth, Australia, 2010.

[67] S. Hirose, J. D. Achenbach, Higher harmonics in the far field due to dynamic crack-face contacting, Journal of the Acoustical Society of America 93 (1) (1993) 142–147.

[68] S. Hirose, 2-D scattering by a crack with contact-boundary conditions, Wave Motion 19 (1993) 37–49.

[69] B. Sarens, B. Verstraeten, C. Glorieux, G. Kalogiannakis, D. Van Hemelrijck, Investigation of contact acoustic nonlinearity in delaminations by shearographic imaging, laser doppler vibrometric scanning and finite difference modeling, Ultrasonics, Ferroelectrics and Frequency Control, IEEE Transactions on 57 (6) (2010) 1383–1395.

[70] K. Kimoto, Y. Ichikawa, A finite difference method for elastic wave scattering by a planar crack with contacting faces, Wave Motion 52 (2015) 120–137.

[71] S. Delrue, K. Van Den Abeele, Three-dimensional finite element simulation of closed delaminations in composite materials, Ultrasonics 52 (2) (2012) 315–324.

[72] L. Baillet, T. Sassi, Mixed finite element methods for the {S}ignorini problem with friction, Numerical Methods for Partial Differential Equations 22 (6) (2006) 1489–1508.

[73] L. Baillet, T. Sassi, Mixed finite element formulation in large deformation frictional contact problem, Revue Européenne des Eléments Finis 14 (2-3) (2005) 287–304.

[74] P. Belanger, P. Cawley, F. Simonetti, Guided wave diffraction tomography within the born approximation, IEEE Transactions on Ultrasonics, Ferroelectrics, and Frequency Control 57 (6) (2010) 1405–1418.

[75] P. Huthwaite, F. Simonetti, High-resolution guided wave tomography, Wave Motion 50 (5) (2013) 979–993.

[76] P. Huthwaite, Evaluation of inversion approaches for guided wave thickness mapping, Proceedings of the Royal Society of London A: Mathematical, Physical and Engineering Sciences 470 (2166) (2014) 20140063–20140063.

[77] X. Zhao, H. Gao, G. Zhang, B. Ayhan, F. Yan, C. Kwan, J. L. Rose, Active health monitoring of an aircraft wing with embedded piezoelectric sensor/actuator network: I. Defect detection, localization and growth monitoring, Smart Materials and Structures 16 (4) (2007) 1208.

[78] J. K. Van Velsor, H. Gao, J. L. Rose, Guided-wave tomographic imaging of defects in pipe using a probabilistic reconstruction algorithm, Insight-Non-Destructive Testing and Condition Monitoring 49 (9) (2007) 532–537.

[79] M. Abramowitz, I. A. Stegun, Others, Handbook of mathematical functions, Vol. 1046, Dover New York, 1965.

[80] N. J. Carpenter, R. L. Taylor, M. G. Katona, Lagrange constraints for transient finite element surface contact, International Journal for Numerical Methods in Engineering 32 (1) (1991) 103–128.

[81] L. L. Thompson, A review of finite-element methods for time-harmonic acoustics, Journal of the Acoustical Society of America 119 (3) (2006) 1315–1330.

[82] P. G. Ciarlet, The finite element method for elliptic problems, Elsevier, 1978.

[83] H. Sohn, S. J. Lee, Lamb wave tuning curve calibration for surface-bonded piezoelectric transducers, Smart Materials and Structures 19 (1) (2010) 15007.

[84] S. Biwa, S. Hiraiwa, E. Matsumoto, Pressure-Dependent Stiffnesses and Nonlinear Ultrasonic Response of Contacting Surfaces, Journal of Solid Mechanics and Materials Engineering 3 (1) (2009) 10–21.